nature portfolio

https://doi.org/10.1038/s41560-021-00952-0

Supplementary information

High areal capacity, long cycle life 4 V ceramic all-solid-state Li-ion batteries enabled by chloride solid electrolytes

In the format provided by the authors and unedited

Supporting Information for:

High areal capacity, long cycle life 4 V ceramic all-solid-state Li-ion batteries enabled by chloride solid electrolytes

Laidong Zhou, [1, 2] *Tong-Tong Zuo,* [3] *Chun Yuen Kwok,* [1] *Se Young Kim,* [1] *Abdeljalil Assoud,* [1] *Qiang Zhang,* [4] *Jürgen Janek,* [3] *Linda F. Nazar* [1, 2]*

[1] Department of Chemistry and the Waterloo Institute for Nanotechnology, University of Waterloo, 200 University Avenue West, Waterloo, Ontario N2L 3G1, Canada

[2] Joint Center for Energy Storage Research, Argonne National Laboratory, Argonne, IL 60439, USA

[3] Institute of Physical Chemistry and Center for Materials Research, Justus Liebig University, Heinrich-Buff-Ring 17, Gießen 35392, Germany

[4] Neutron Scattering Division, Oak Ridge National Laboratory, Oak Ridge, Tennessee 37830, United States

Corresponding Author

*E-mail: lfnazar@uwaterloo.ca

LIST OF SUPPLEMENTAL FIGURES

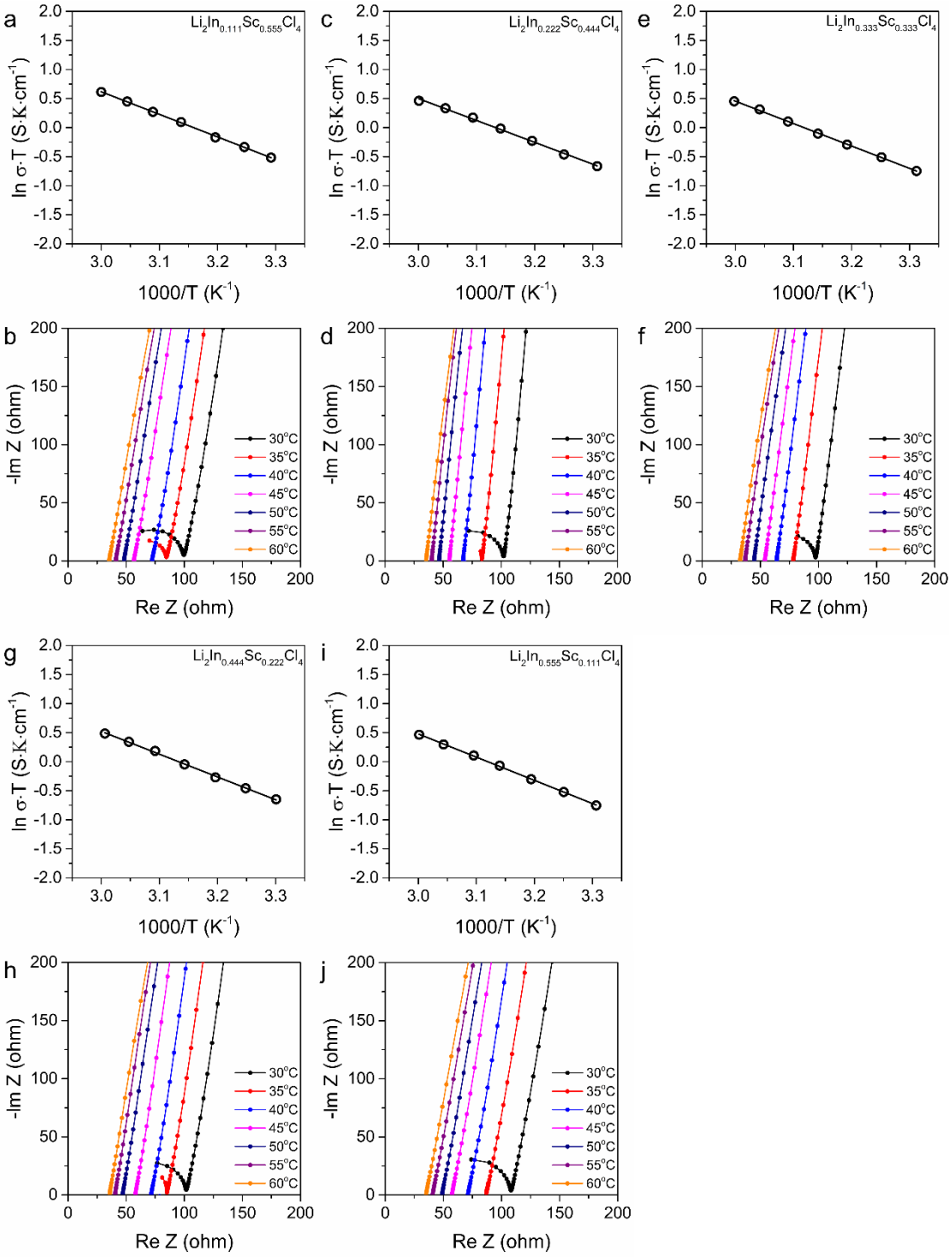

Supplementary Figure 1. Arrhenius plots for (a) $Li_2In_{0.111}Sc_{0.555}Cl_4$; (c) $Li_2In_{0.222}Sc_{0.444}Cl_4$; (e) $Li_2In_{0.333}Sc_{0.333}Cl_4$; (g) $Li_2In_{0.444}Sc_{0.222}Cl_4$ and (i) $Li_2In_{0.555}Sc_{0.111}Cl_4$ in the temperature range from 30 to 60 °C. Corresponding Nyquist plots of (b) $Li_2In_{0.111}Sc_{0.555}Cl_4$; (d) $Li_2In_{0.222}Sc_{0.444}Cl_4$; (f) $Li_2In_{0.333}Sc_{0.333}Cl_4$; (h) $Li_2In_{0.444}Sc_{0.222}Cl_4$ and (j) $Li_2In_{0.555}Sc_{0.111}Cl_4$ at each temperature used in the Arrhenius plots.

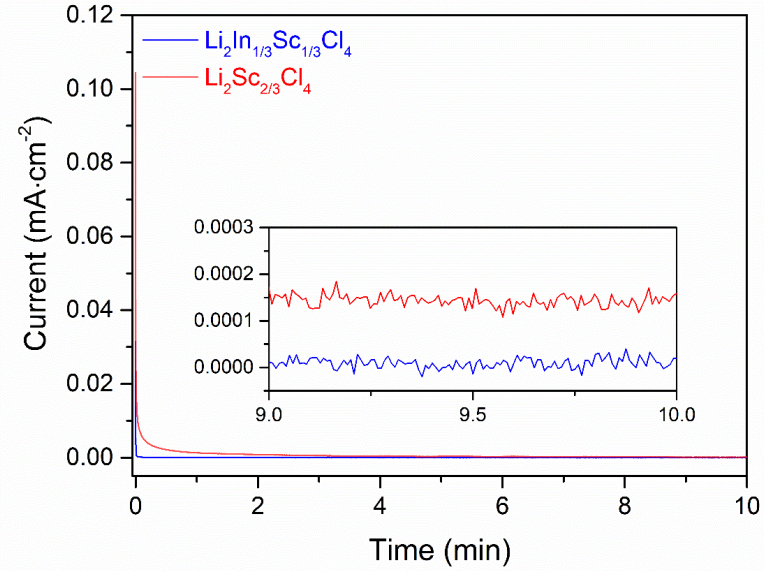

Supplementary Figure 2. Comparison of electronic conductivity of $Li_2In_{1/3}Sc_{1/3}Cl_4$ and $Li_2Sc_{2/3}Cl_4$ measured by the DC polarization method. Chronoamperometry result for the stainless steel | SE | stainless steel cells with constant voltage of 1 V; the corresponding electronic conductivity of $Li_2In_{1/3}Sc_{1/3}Cl_4$ (blue curve) is 4.7 x 10^{-10} S·cm^{-1} and $Li_2Sc_{2/3}Cl_4$ (red curve) is 4.2 x 10^{-9} S·cm^{-1}.

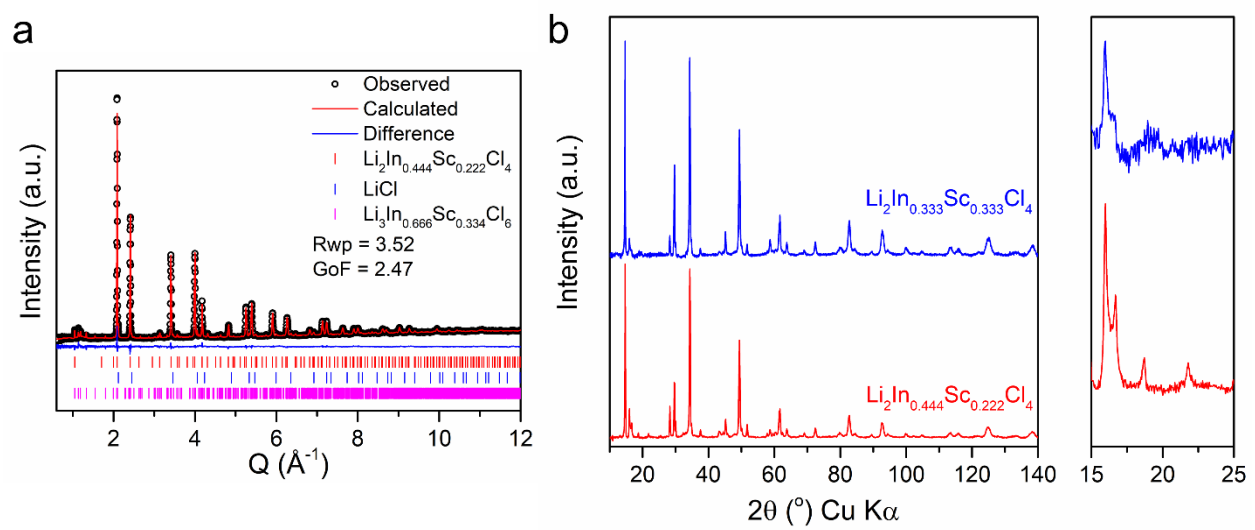

Supplementary Figure 3. (a) Time-of-flight neutron diffraction pattern and the corresponding Rietveld refinement of $Li_2In_{0.444}Sc_{0.222}Cl_4$, Experimental data are shown in black circles; the red line denotes the calculated pattern; the difference profile is shown in blue and calculated positions of the Bragg reflections are shown as red ($Li_2In_{0.444}Sc_{0.222}Cl_4$, 58.78%), blue (LiCl, 1.82%) and pink ($Li_3In_{0.666}Sc_{0.334}Cl_6$, 39.40%) vertical ticks. R_{wp} and *GoF* are the weighted profile *R*-factor and goodness of fit respectively. Due to the peak overlap between the cubic spinel and monoclinic phases, the refinement was initially conducted with only the cubic spinel phase and LiCl, and then all the structural parameters were fixed. Finally, the monoclinic phase was added to the refinement, with the single crystal diffraction framework used as a starting point. The Sc and In occupancies were fixed from single crystal results during the refinement. (b) powder X-ray diffraction patterns collected in Debye-Scherrer geometry, of $Li_2In_{0.444}Sc_{0.222}Cl_4$ (red), and $Li_2In_{0.333}Sc_{0.333}Cl_4$ (blue) at high-resolution with long scan times to identify trace impurities. Samples were sealed in 0.3 mm (diameter) glass capillaries under argon. The enlarged area shows reflections corresponding to the monoclinic phase, which is almost invisible for $Li_2In_{0.333}Sc_{0.333}Cl_4$.

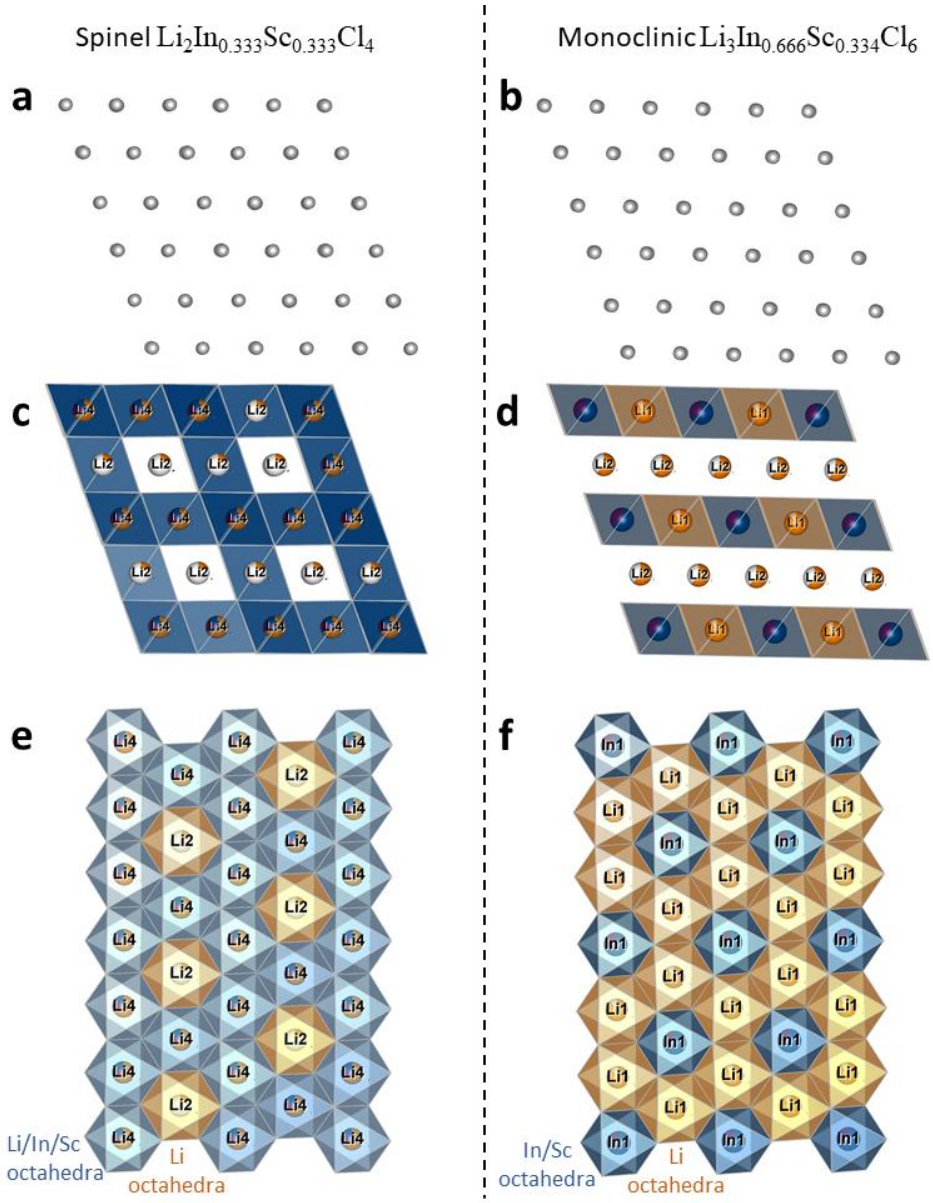

Supplementary Figure 4. Structural comparison between spinel $Li_2In_{0.333}Sc_{0.333}Cl_4$ and monoclinic $Li_3In_{0.666}Sc_{0.334}Cl_6$. (a, b) a cubic close-packed (ccp)-like Cl anion arrangement in both structures; (c) spinel structure with Sc/In occupying sites in the Li layer, and (d) monoclinic structure with no Sc/In in Li layer; (e) spinel structure with Sc/In/Li shared site, and (f) monoclinic structure with distinct In/Sc and Li sites (no shared occupancy).

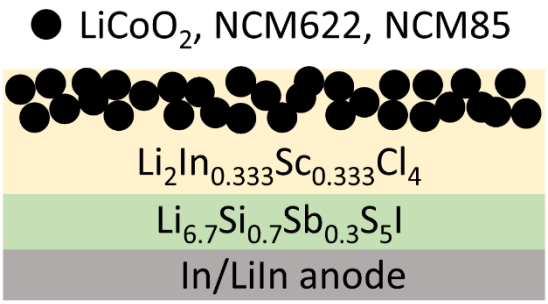

Supplementary Figure 5. Schematic illustration of the ASSB configuration, with In/LiIn as the negative electrode, $Li_{6.7}Si_{0.7}Sb_{0.3}S_5I$ as the separator and $Li_2In_{0.333}Sc_{0.333}Cl_4$ as the solid electrolyte for the cathode composite and separator.

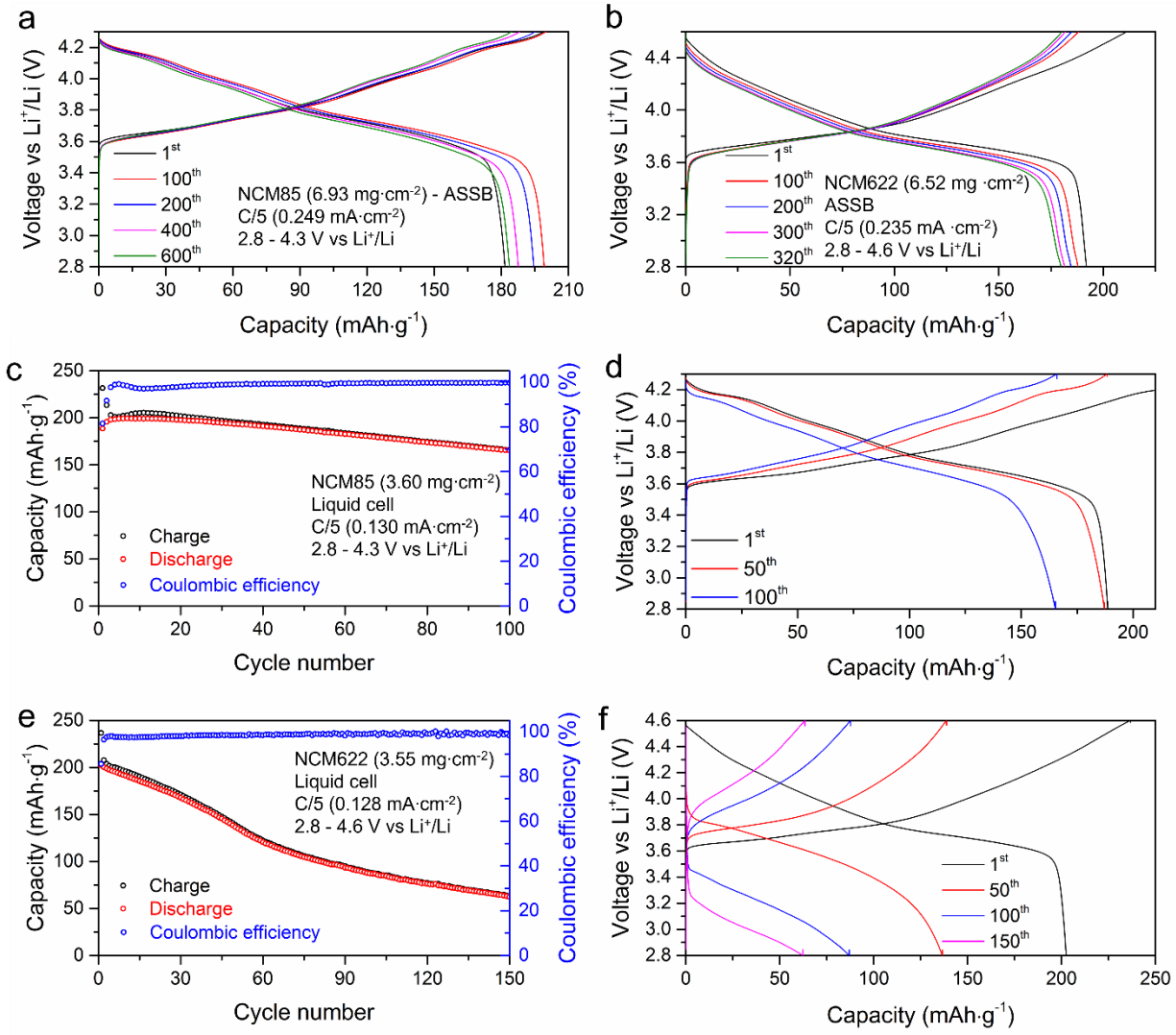

Supplementary Figure 6. Charge-discharge voltage profile of an NCM85 (a) ASSB cycled at a C/5 rate between 2.8 - 4.3 V vs Li^+/Li; and an NCM622 (b) ASSB cycled at C/5 rate between 2.8 - 4.6 V vs Li^+/Li. Charge-discharge capacity and the coulombic efficiency (CE) as a function of cycle number and corresponding charge-discharge voltage profile for a NCM85 (c, d) liquid cell cycled at C/5 rate between 2.8 - 4.3 V vs Li^+/Li; and a NCM622 (e, f) liquid cell cycled at C/5 rate between 2.8 - 4.6 V vs Li^+/Li. This demonstrates the superior stable cycling of the ASSB compared to the conventional liquid cell.

Supplementary Note 1. The liquid cells use a standard organic liquid electrolyte (LP57; 1 M $LiPF_6$ in EC/EMC) and Li metal. Thus, the capacity fade partially originates from the Li anode due to SEI formation, in addition to electrolyte decomposition on the surface of NCM which occurs above 3.8 V vs Li^+/Li.[1] Other liquid electrolytes with different solvent and Li salt have been developed which exhibit much better electrochemical performance,[2,3,4] but are not commercially available.

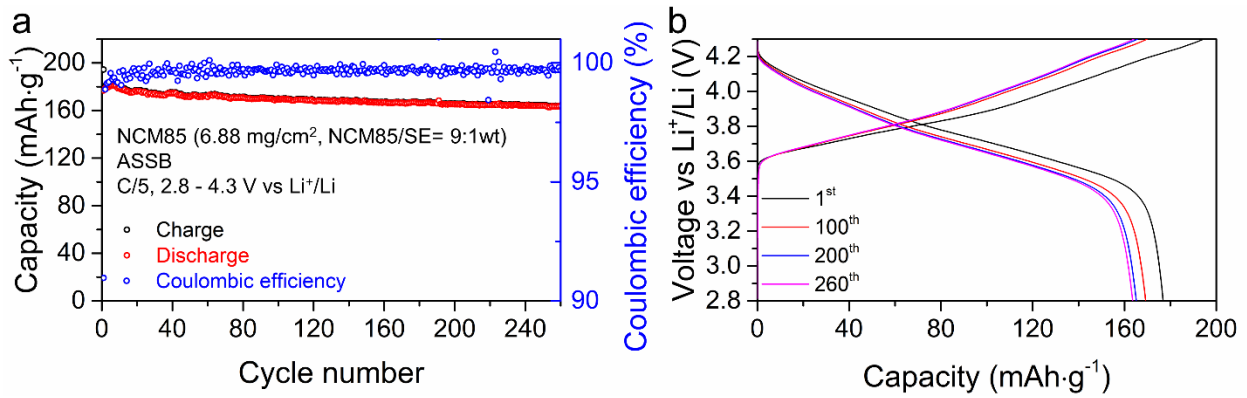

Supplementary Figure 7. Charge-discharge capacity and the coulombic efficiency as a function of cycle number for (a) NCM85 ASSB with a cathode composite weight ratio of NCM85 and $Li_2In_{1/3}Sc_{1/3}Cl_4$ solid electrolyte of 90:10, (b) corresponding charge-discharge voltage profiles.

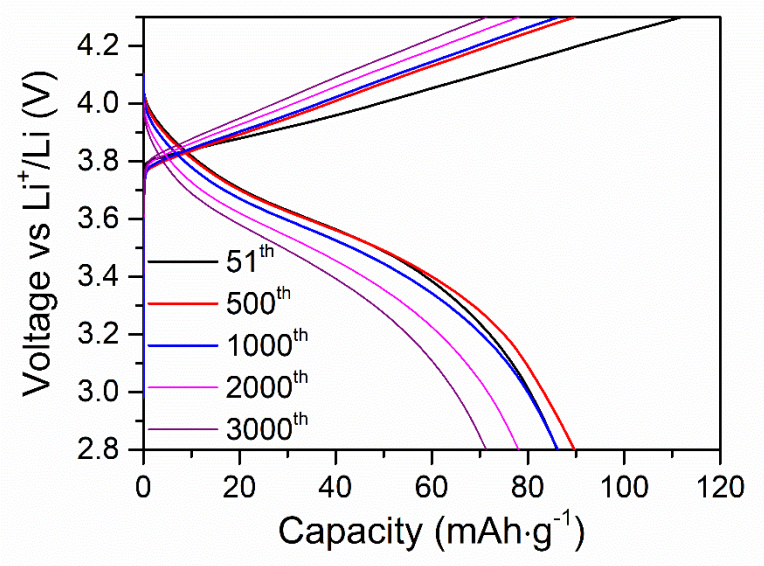

Supplementary Figure 8. Charge-discharge voltage profiles of long-term cycling of the NCM85 ASSB (after rate cycling) at 3C, demonstrating excellent cycling stability over more than 3000 cycles.

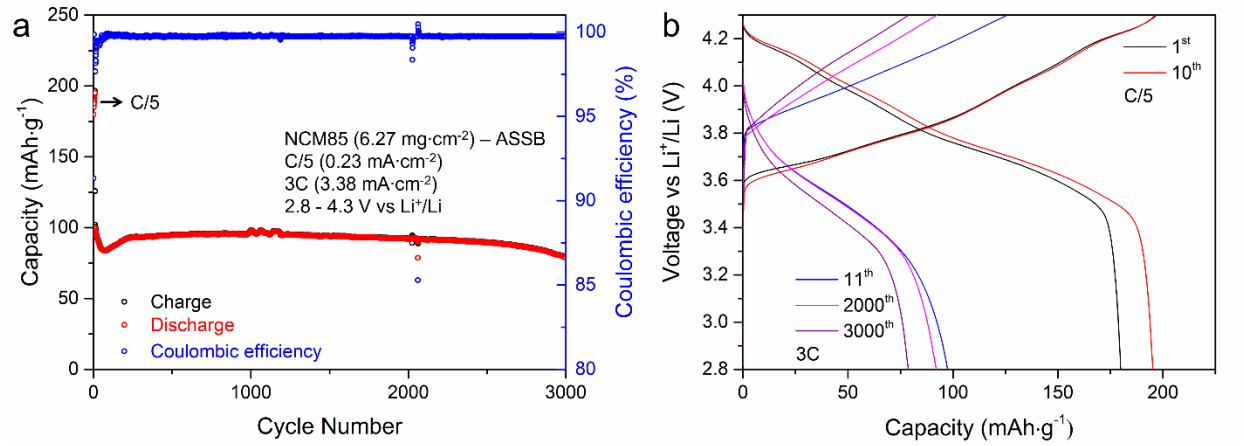

Supplementary Figure 9. (a) Charge-discharge capacity and coulombic efficiency as a function of cycle number and (b) Charge-discharge voltage profiles for NCM85 ASSB cycled at 3C rate between 2.8 - 4.3 V vs Li^+/Li, with initial 10 cycles cycled at C/5.

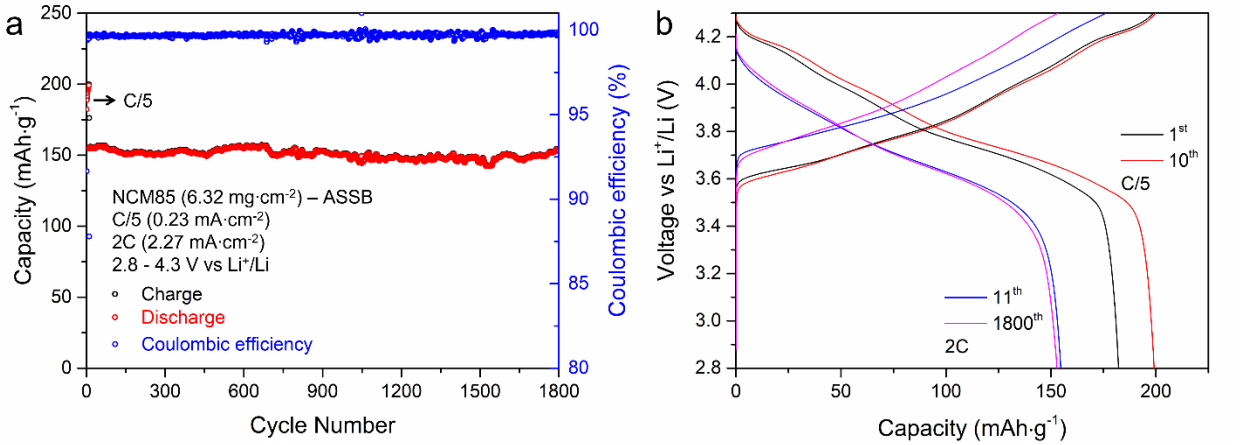

Supplementary Figure 10. (a) Charge-discharge capacity and the coulombic efficiency as a function of cycle number and (b) Charge-discharge voltage profiles for NCM85 ASSB cycled at a 2C rate between 2.8 - 4.3 V vs Li^+/Li, with the initial 10 cycles cycled at C/5. Small fluctuations in capacity and CE in (a) are due to temperature variation during cycling.

Supplementary Note 2. The In/InLi anode was made by pressing together an In foil (thickness of 100 µm, diameter of 10 mm) and a Li foil (~ 1 mg). The initial 10 cycles at low current density are essential to form the In/LiIn two-phase anode and create a stable interface between the anode and the argyrodite solid electrolyte. Thus, the cells (Supplementary Figure 9, 10) exhibit higher discharge capacity than in Figure 3c,d at same rate (i.e., current density). As the cells used for rate cycling were only cycled at low current density for 5 cycles, the cell performance at high rate is limited by the limited reversibility of the In/LiIn two-phase anode.[5]

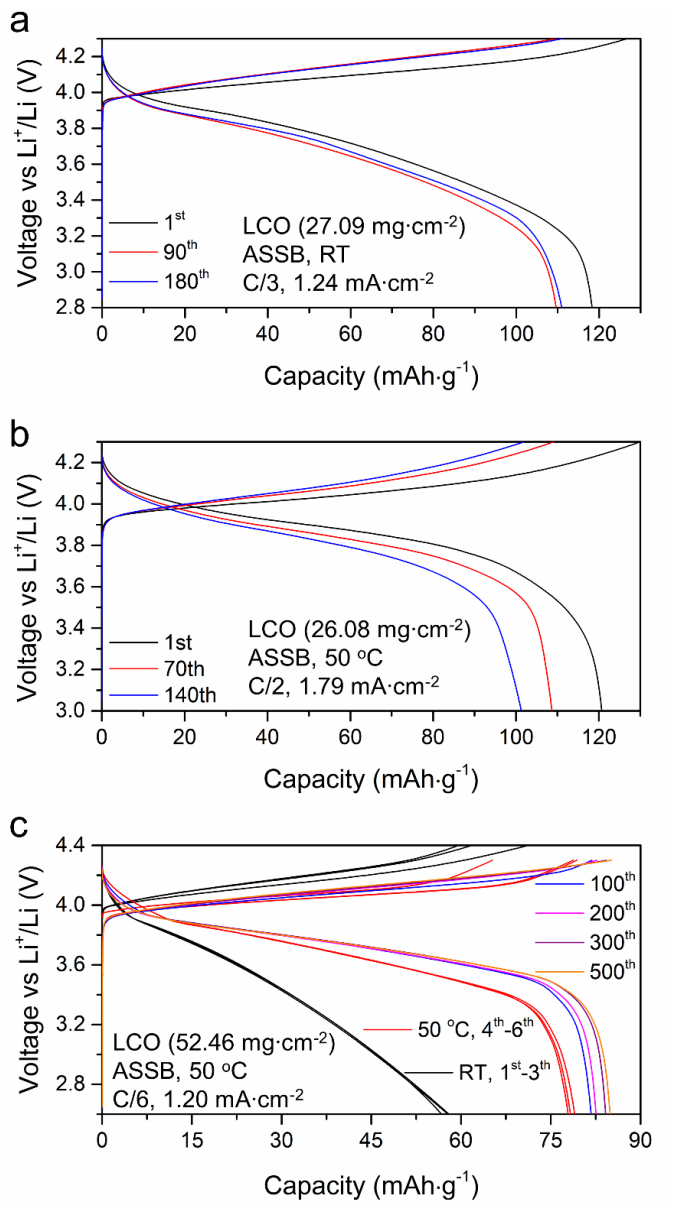

Supplementary Figure 11. Charge-discharge voltage profiles of high-loading long-term cycling of LCO ASSBs at (a) room temperature (RT), cycled at C/3 between 2.8 V - 4.3 V vs Li^+/Li and (b) 50 °C, cycled at C/2 between 3.0 V - 4.3 V vs Li^+/Li and of (c) ultra-high-loading LCO ASSB cycled at a C/6 rate and room temperature between 2.6 V - 4.4 V vs Li^+/Li and 50 °C between 2.6 V - 4.3 V vs Li^+/Li. At high cathode active material loadings, the kinetics of Li ion/electron diffusion within the thick cathode composite are more limited than at low loadings. At high current densities, that results in a high overpotential. The ionic conductivity of the solid electrolyte and both ionic/electronic conductivity of cathode active materials increases with increasing temperature, thus giving better Li ion/electron diffusion kinetics and lower overpotentials. In short, a wider cut-off potential window was used for high-loading ASSB cycled at RT.

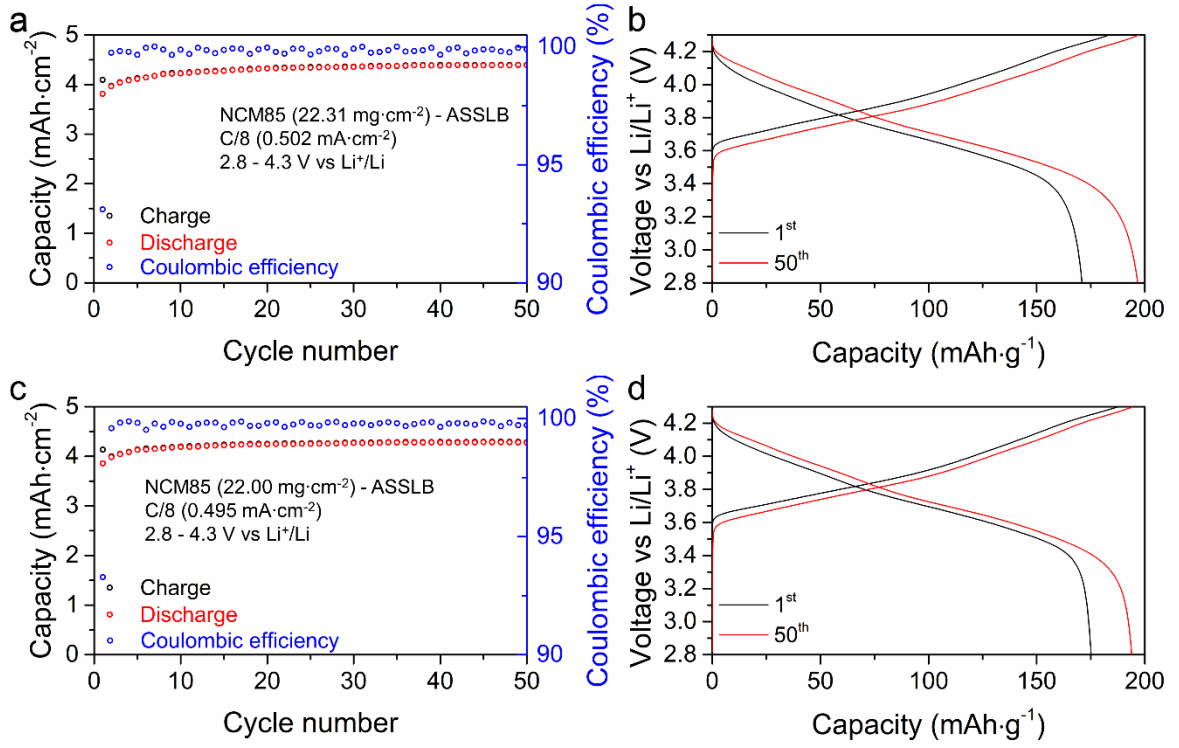

Supplementary Figure 12. High loading NCM85 ASSBs with 22.31 and 22.00 mg·cm^{-2} CAM-loading cycled at room temperature between 2.8 - 4.3 V vs Li^+/Li at a C/8 rate and the corresponding charge-discharge curves. The data, which are essentially the same as shown in Figure 5d,e, demonstrate reproducibility of the electrochemical performance.

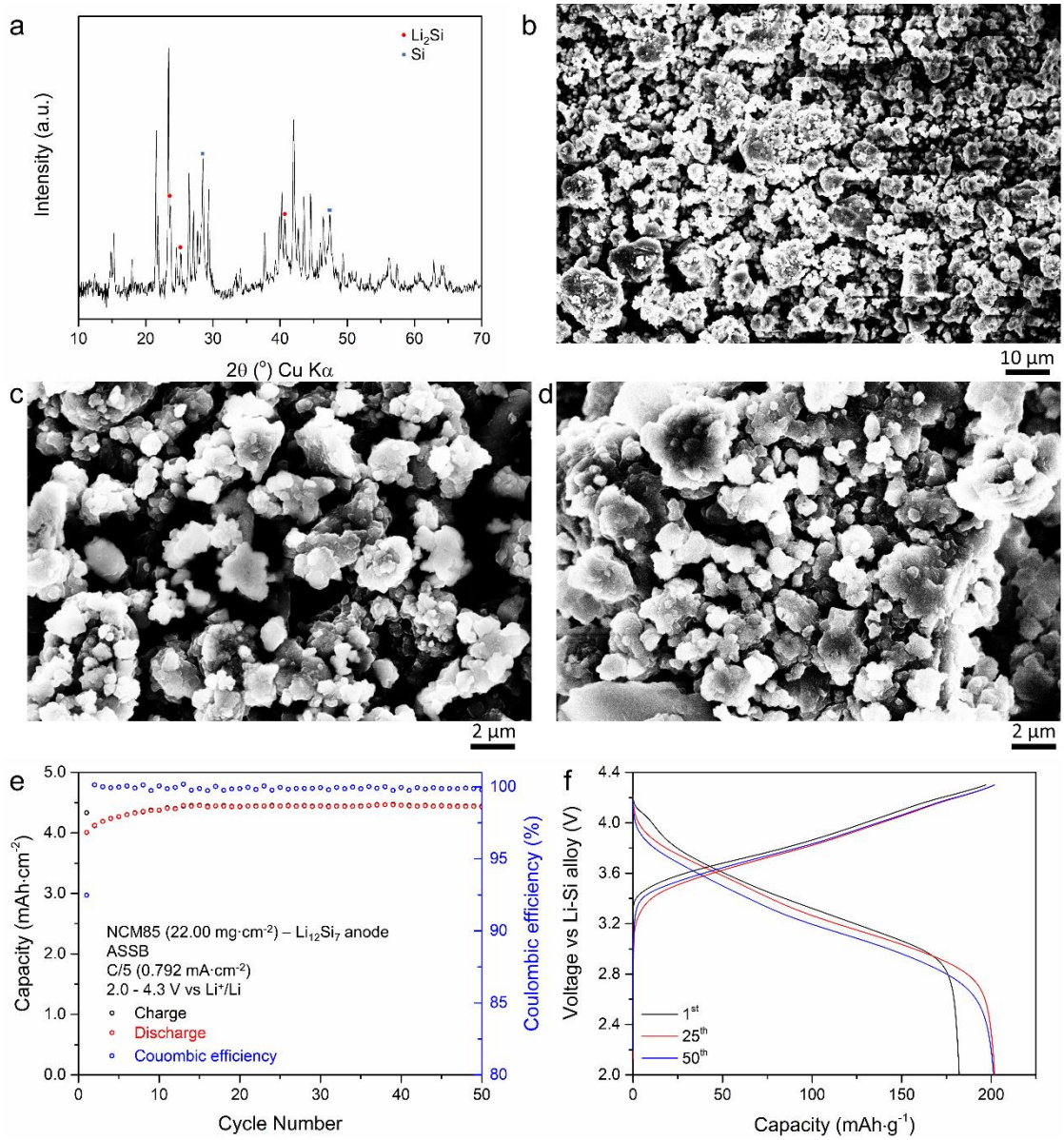

Supplementary Figure 13. (a) XRD pattern of a Li-Si alloy synthesized by mixing Li and Si powder; the main reflections are assigned to $Li_{12}Si_7$ and residual Si and Li_2Si are indicated. (b-d) SEM images of the as-synthesized Li-Si alloy showing micron-sized particles. (e) Charge-discharge capacity and the coulombic efficiency as a function of cycle number and (f) Charge-discharge voltage profiles for NCM85 ASSB with the Li-Si alloy anode cycled at a C/5 rate between 2.0 - 4.3 V.

Supplementary Note 3. Silicon powder (99%, Sigma-Aldrich, 325 mesh) was ball milled at 400 rpm for 10 hours to reduce the particle size. Stoichiometric amounts of the ball-milled Si powder and Li powder (FMC) (corresponding to the target phase $Li_{12}Si_7$) were gently mixed, and then ground in an agate mortar until a homogeneous black colored powder was obtained. The NCM85 ASSB was fabricated using the same procedure as for the cell with In/InLi (see Supplementary Figure 12), using 21.6 mg cathode composite loading and 3.5 mg $Li_{12}Si_7$ powder as the anode.

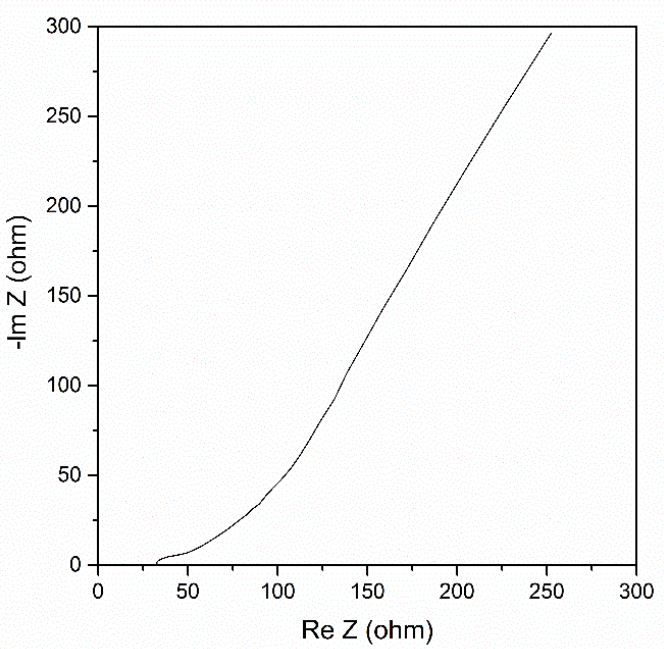

Supplementary Figure 14. Initial Nyquist plot of the NCM622 ASSB corresponding to the first point on the charge curve (point 1) in Figure 6a.

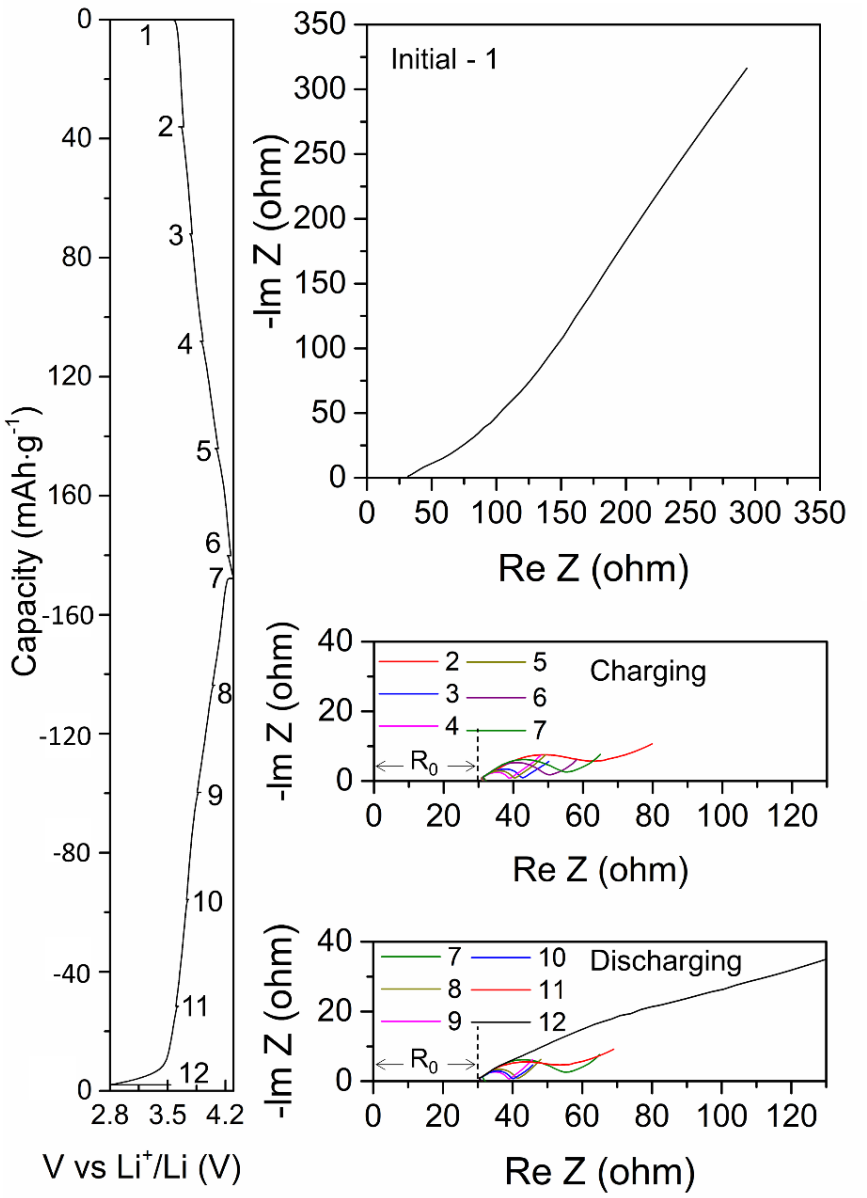

Supplementary Figure 15. Impedance evolution during the first cycle of an NCM85 ASSB cycled between 2.8 - 4.3 V vs Li^+/Li. The corresponding voltage profile (left) and impedance spectra (right) collected on the first cycle (top); during charging (middle) and discharging (bottom) are shown. The numbers on the voltage profile correspond to the points where the EIS spectra were collected at every hour after a 30 min rest (before and after). All studies were conducted at a C/5 rate.

EIS spectra were measured in two-electrode configuration as we only sought to monitor the overall impedance changes in these studies; three electrode cells will be described in forthcoming work. The spectra could not be fit reliably with equivalent circuits owing to the complexity of the impedance response and overlapping contributions. The value of R_0 (~ 30 ohm) corresponds well to the resistance drop from the solid electrolyte separator as estimated from the conductivity and thickness.

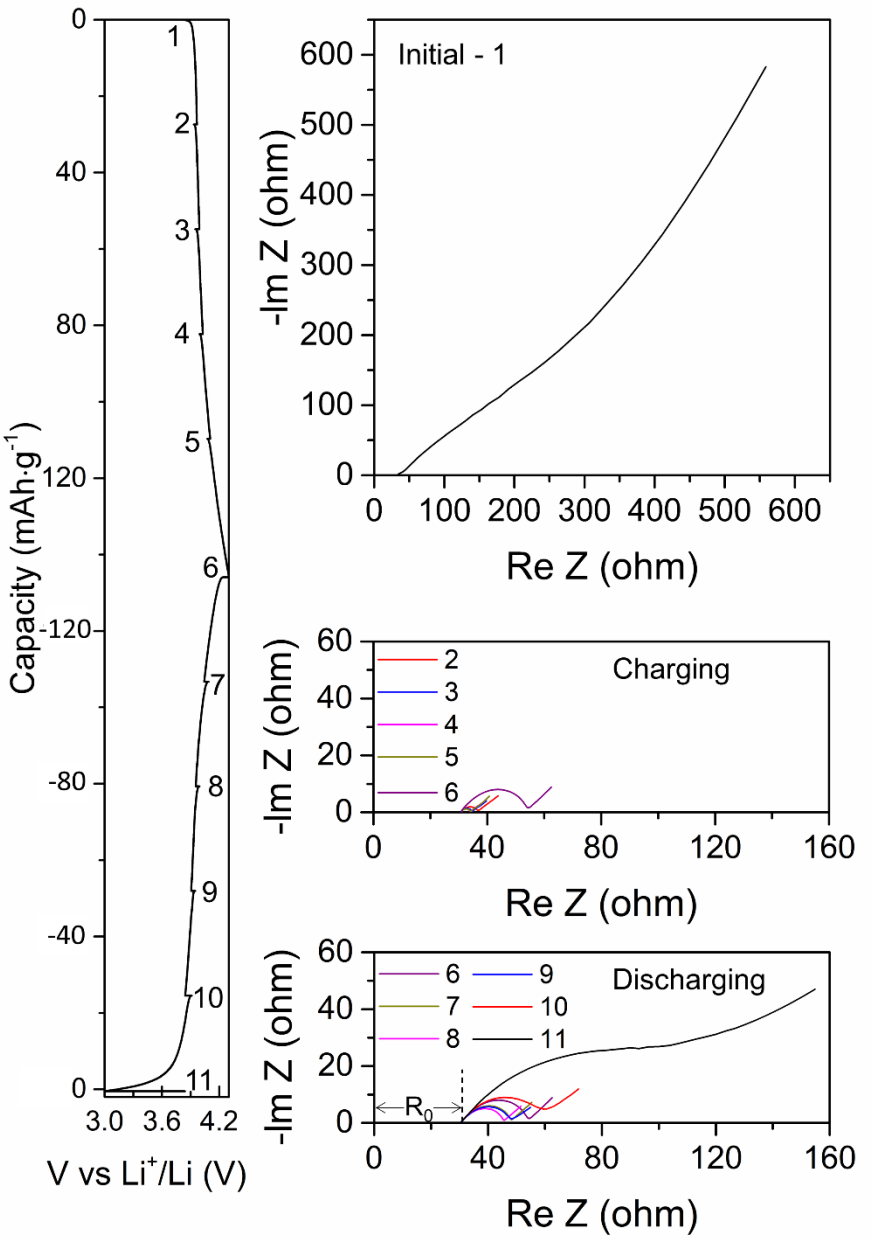

Supplementary Figure 16. Impedance evolution during the first cycle of a LCO ASSB cycled between 3.0 - 4.3 V vs Li^+/Li. The corresponding voltage profile (left) and impedance spectra (right) collected on the first cycle (top); during charging (middle) and discharging (bottom) are shown. The numbers on the voltage profile correspond to the points where the EIS spectra were collected at every hour after a 30 min rest (before and after). All studies were conducted at a C/5 rate.

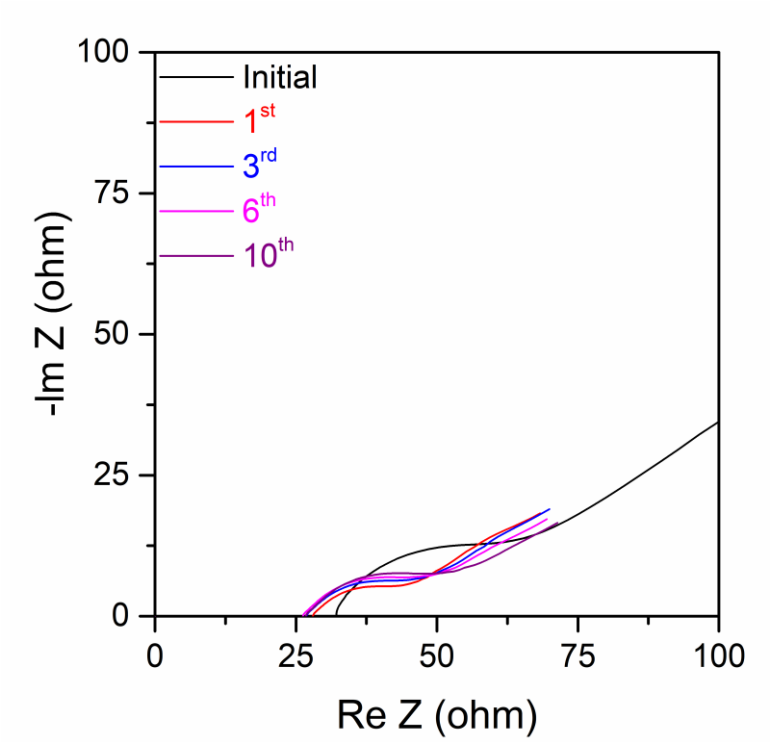

Supplementary Figure 17. Nyquist plots of the fully discharged LCO ASSB cycled at a C/2 rate between 2.8 - 4.3 V vs Li^+/Li, shown over the first 10 cycles.

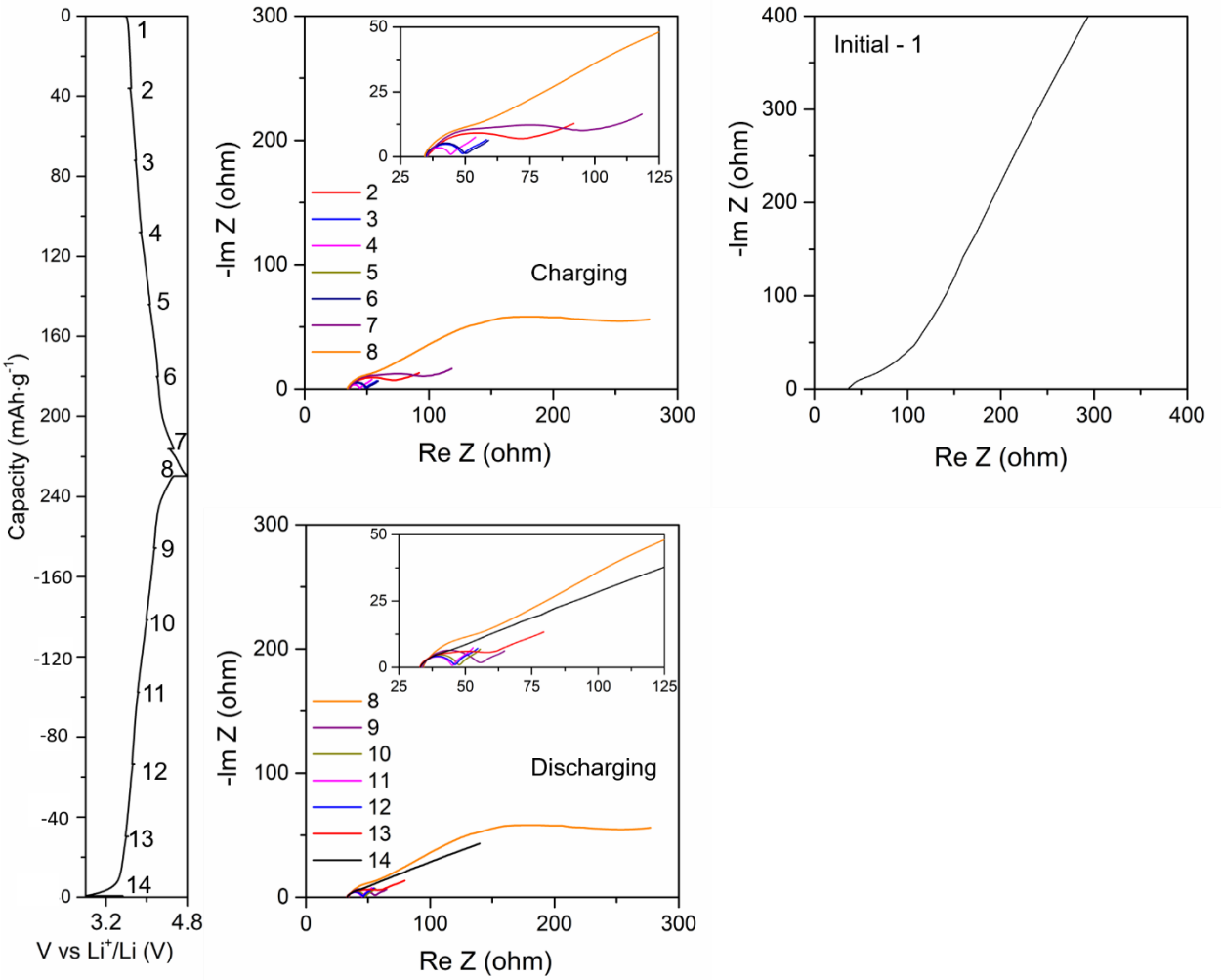

Supplementary Figure 18. Impedance evolution during the first cycle of a NCM85 ASSB cycled between 2.8 - 4.8 V vs Li^+/Li. The corresponding voltage profile (left) and impedance spectra (right) collected in the first cycle; during charging (middle top), discharging (middle bottom) and initial (right) are shown. The numbers on the voltage profile correspond to the points where the EIS spectra were collected at every hour after a 30 min rest (before and after). All studies were conducted at a C/5 rate.

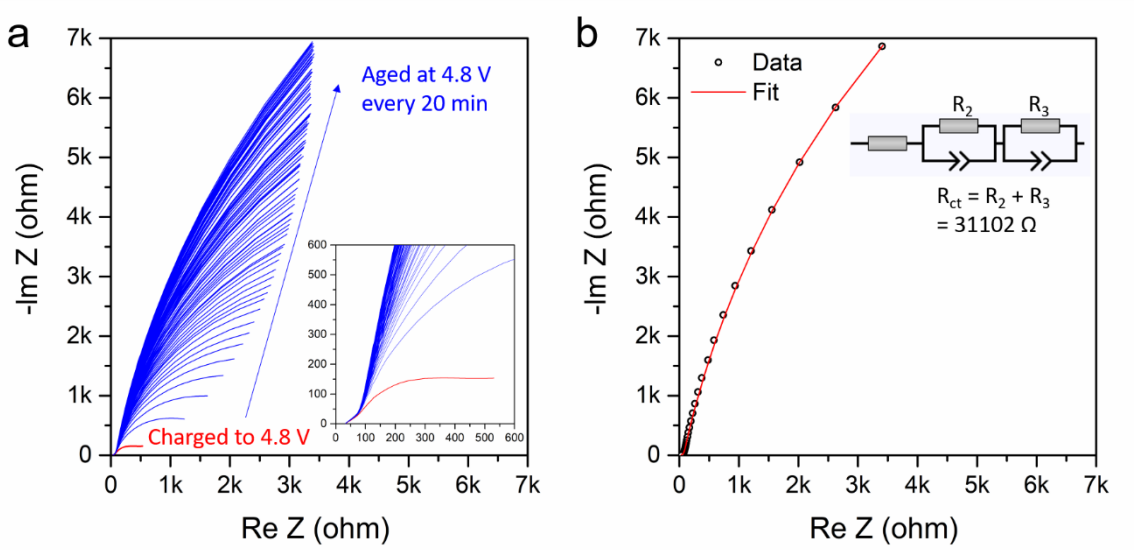

Supplementary Figure 19. (a) Impedance evolution at high-voltage, where the EIS spectra were collected every 20 min of "aging" at a constant applied potential of 4.8 V vs Li^+/Li. (b) Equivalent circuit fit of the final Nyquist plot of NCM85 ASSB after 30 h aging at 4.8 V vs Li^+/Li, which shows increased charge transfer resistance between NCM85 and $Li_2In_{1/3}Sc_{1/3}Cl_4$ due to significantly decreased Li-ion mobility and electronic conductivity in highly de-lithiated NCM85.

Supplementary Note 4. The increased impedance (Supplementary Figure 19) on charging at a constant potential of 4.8 V vs Li^+/Li is caused by the very large drop in electronic conductivity and Li-ion mobility in highly de-lithiated NCM85 ($Li_{0.07}Ni_{0.85}Co_{0.1}Mn_{0.05}O_2$).

In contrast, upon "aging" the cell at a lower potential of 4.3 V, less Li is extracted from NCM85 - *i.e.,* to form $Li_{0.19}Ni_{0.85}Co_{0.1}Mn_{0.05}O_2$ - which exhibits higher Li-ion mobility and electronic conductivity. Thus, a stabilized and much lower impedance is observed (see below, Supplementary Figure 20).

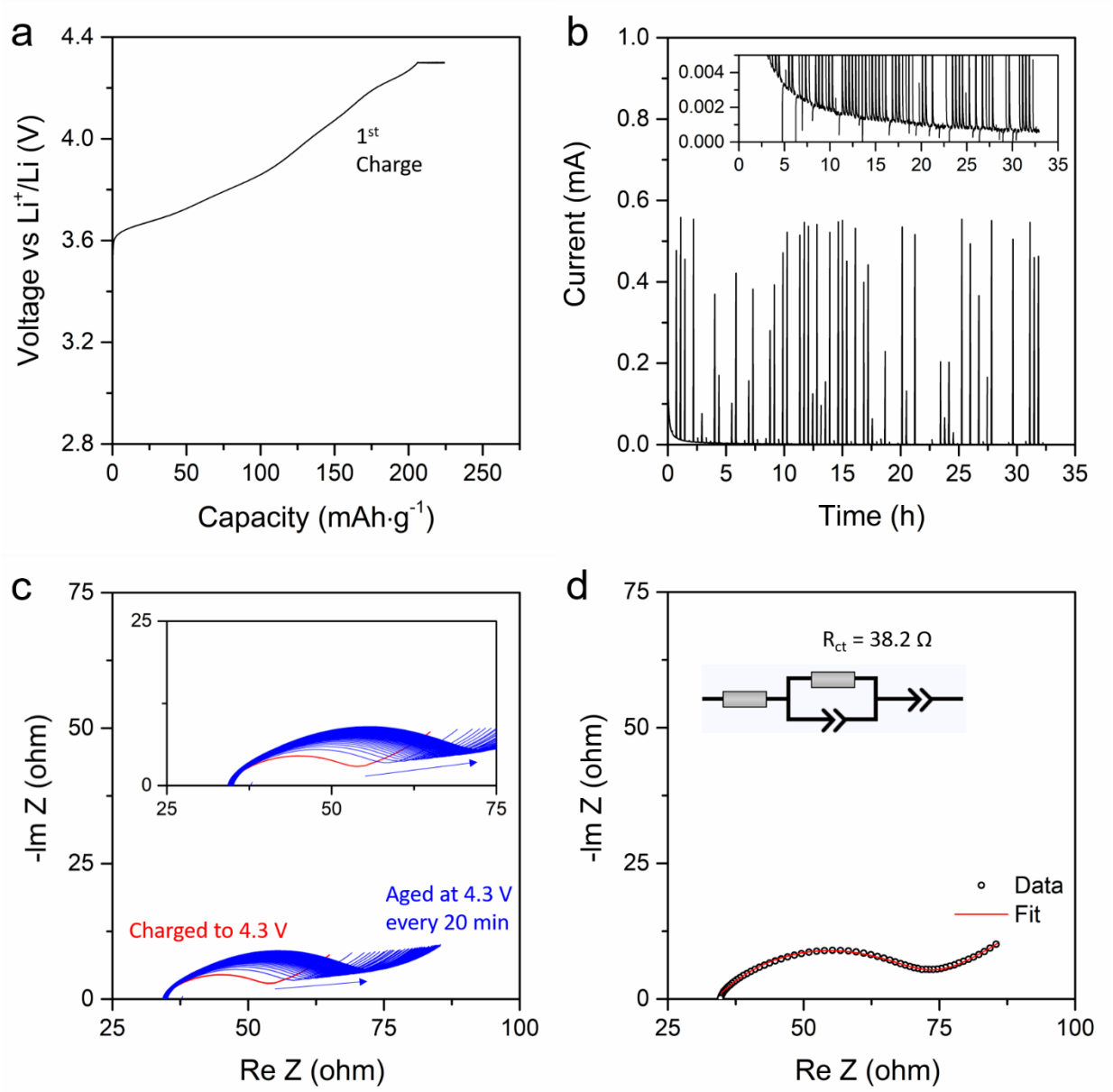

Supplementary Figure 20. (a) Charge voltage profile of NCM85 ASSB. After charging to 4.3 V vs Li^+/Li, the cell was held at that constant potential for 30 h; (b) the corresponding leakage current during the 4.3 V vs Li^+/Li constant voltage hold ("aging"). (c) Impedance evolution during the voltage hold at constant applied potential of 4.3 V vs Li^+/Li, where EIS spectra were collected every 20 min. The lack of significant change in the spectra indicates formation of a stable interface between NCM85 and the chloride SE at this potential. (d) Equivalent circuit fit of the final Nyquist plot of NCM85 ASSB after 30 h "aging" at 4.3 V vs Li^+/Li, which shows very low charge transfer resistance.

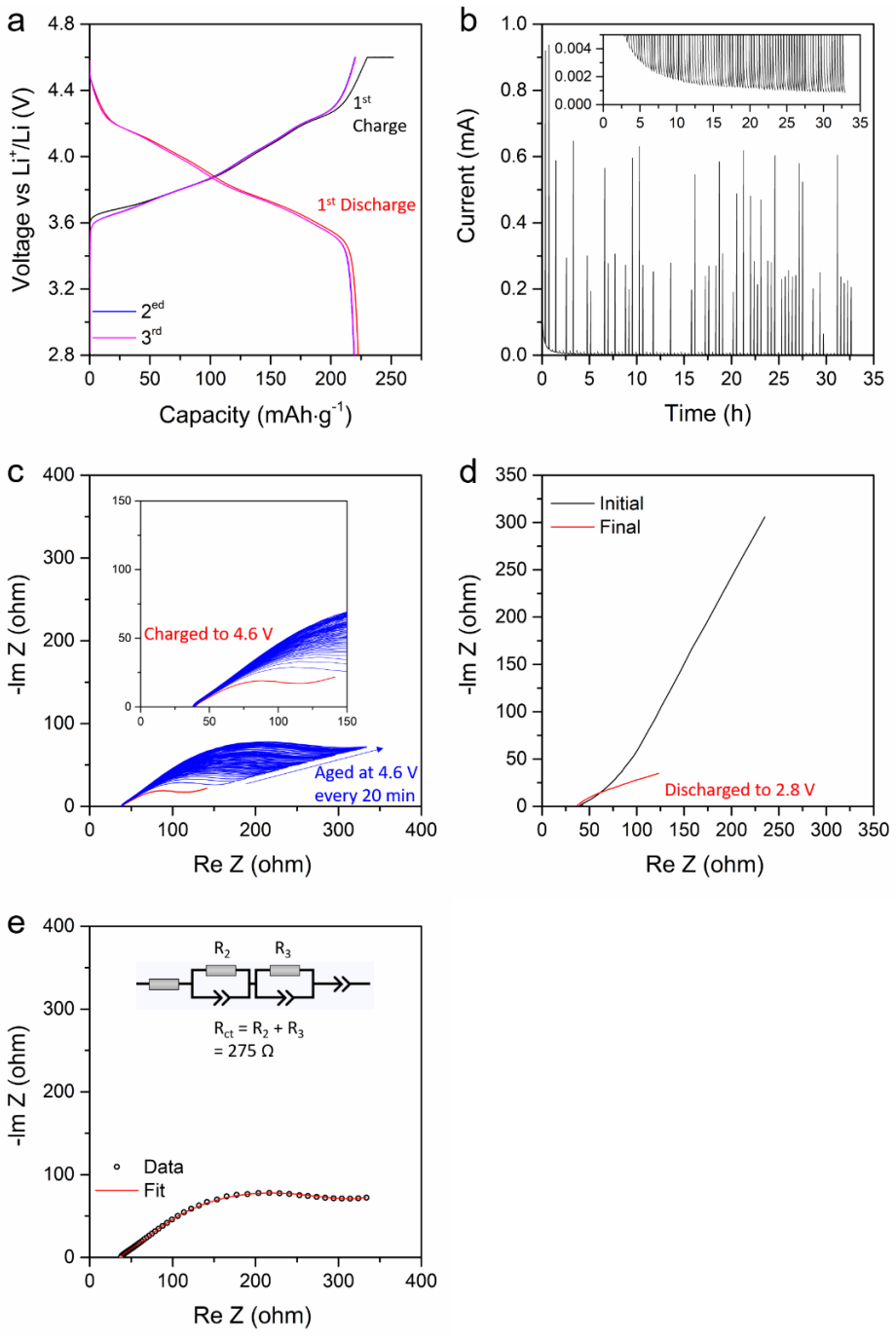

Supplementary Figure 21. (a) Charge-discharge voltage profile of NCM85 ASSB, initial and after two subsequent cycles. After the initial charge to 4.6 V vs Li^+/Li, the cell was held at that potential for 30 h. (b) the corresponding leakage current during the 4.6 V constant hold ("aging") period. (c) Impedance evolution during the voltage hold at 4.6 V vs Li^+/Li, where the EIS spectra were collected every 20 min. (d) Nyquist plots of NCM85 ASSB at initial state, and at 3rd discharge. Upon re-lithiation on discharge, the cell impedance returns to its low value suggesting the formation of a stable interface between NCM85 and the chloride SE. (e) Equivalent circuit fit of the final Nyquist plot of NCM85 ASSB at 4.6 V vs Li^+/Li after the 30 h hold at that potential, showing low charge transfer resistance.

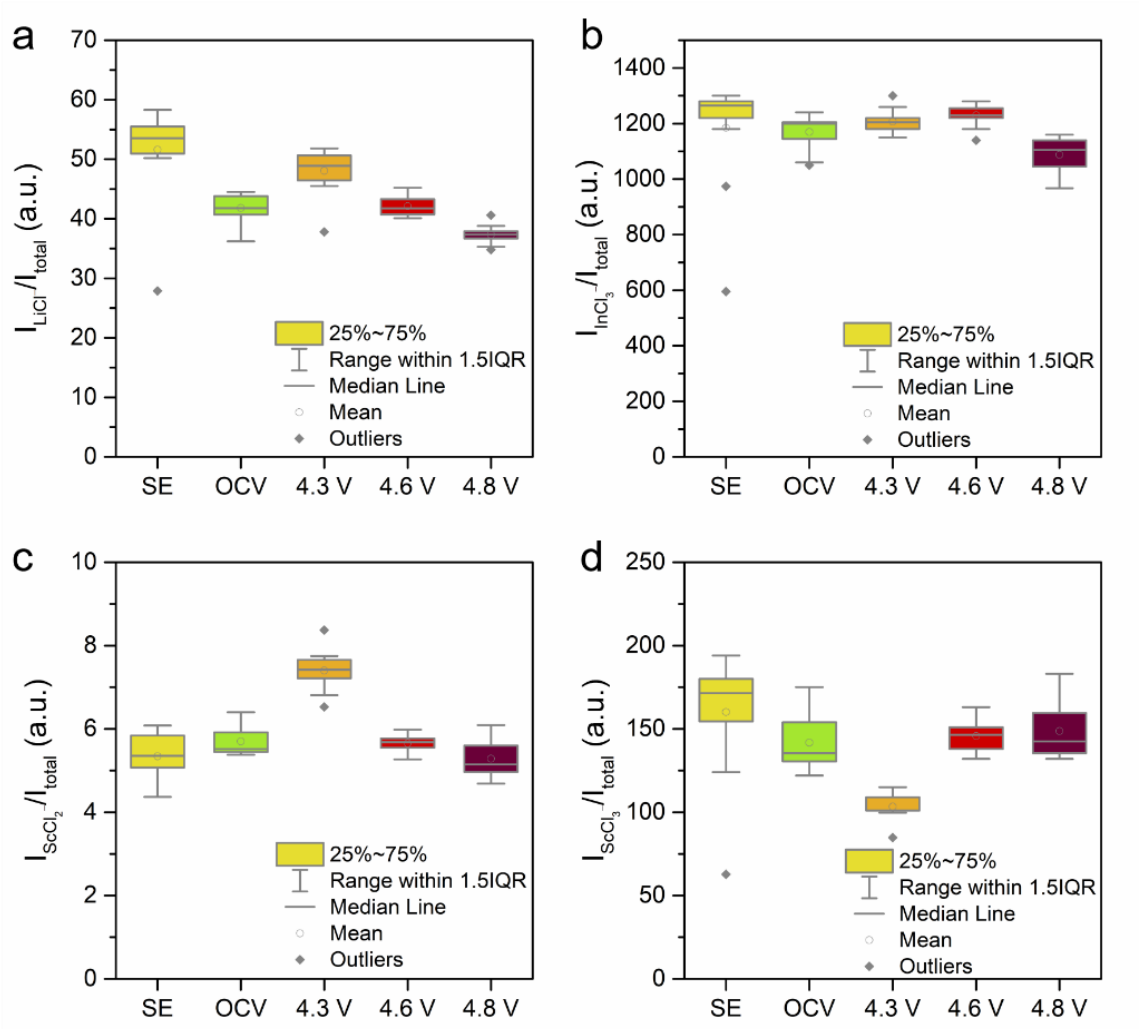

Supplementary Figure 22. TOF-SIMS surface analysis results of (a) $LiCl^-$, (b) $InCl_3^-$, (c) $ScCl_2^-$ and (d) $ScCl_3^-$ fragments of bare SE, uncycled cathode composite and cycled composite with cut-of potential of 4.3 V (160 cycles), 4.6 V (20 cycles) and 4.8 V (10 cycles) vs Li^+/Li. These fragment's signal originate from the chloride SE and show no clear change after cycling, which demonstrate the stable interface at high voltage up to 4.8 V vs Li^+/Li. The box plots were obtained based on the corresponding normalized signal tensities of 12 spectra on each sample. The minima, maxima, median, bounds of box and whiskers, and percentile were provided in Supplementary Table 8.

Supplementary Note 5. The signal intensities of halide fragments (*i.e.*, $LiCl^-$, $InCl_3^-$, $ScCl_2^-$ and $ScCl_3^-$) were compared to evaluate any possible decomposition of the solid electrolyte. There is no pronounced trend in the $LiCl^-$ and $InCl_3^-$ signals. The signal intensity of the $ScCl_2^-$ fragment shows a slight increase for the 4.3 V sample. The $ScCl_3^-$ signal shows a reverse trend with $ScCl_2^-$ signal. This phenomenon may relate to a really minor decomposition process taking place after long term cycling. However, the cell can sustain stable long-term cycling with 90% capacity retention over 600 cycles (Figure 4a), which suggests such minor decomposition does not significantly affect the ASSB performance.

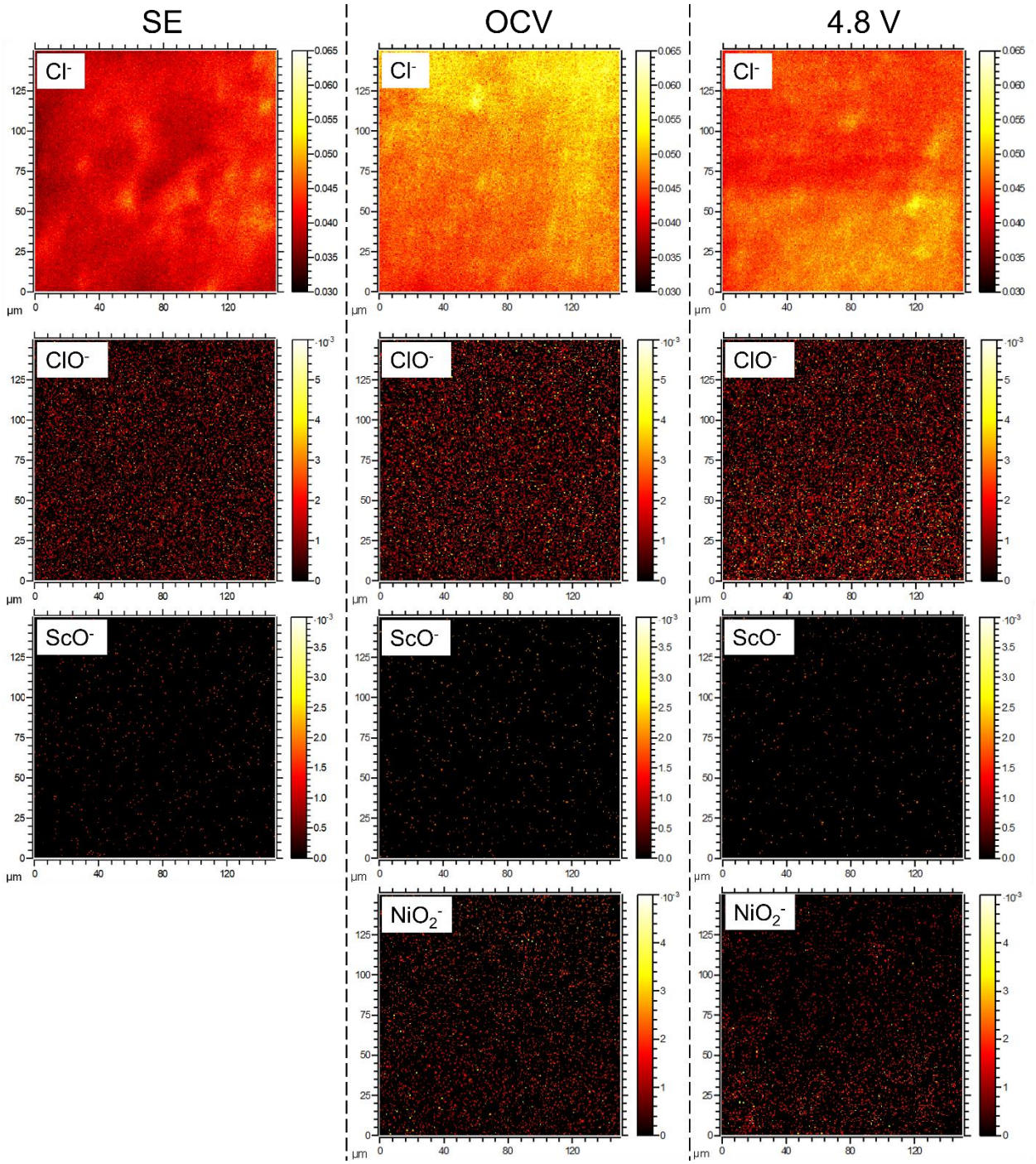

Supplementary Figure 23. TOF-SIMS secondary images of negatively charged fragments: Cl^-, ClO^-, ScO^- and NiO_2^- measured on the top surface of the SE, uncycled cathode composite (OCV) and cycled cathode composite (cycled between 2.8 - 4.8 V vs Li^+/Li) pellets. Color scale unit: a.u.. As the ToF-SIMS images display a large sample area of 150*150 μm^2 which contains numerous NCM85 particles (D50 = 5 µm), numerous SE-NCM85 interfaces can thus be measured to track even minor changes. But the resolution of these images is not enough to identify individual NCM85 particles, which is also not necessary to obtain the analytical information of the degradation products.

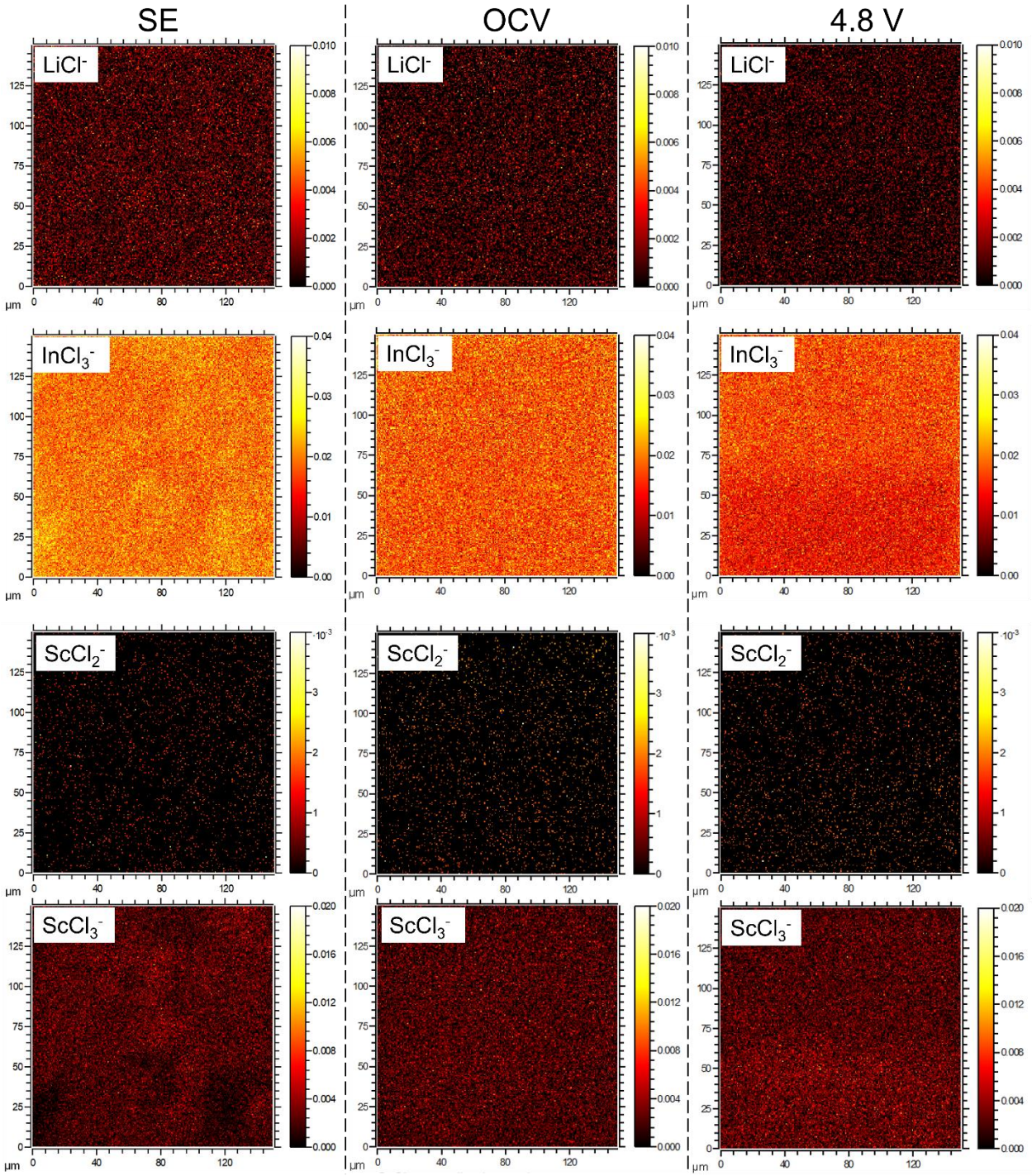

Supplementary Figure 24. TOF-SIMS secondary images of negatively charged fragments: $LiCl^-$, $InCl_3^-$, $ScCl_2^-$ and $ScCl_3^-$ measured on the top surface of the SE, uncycled cathode composite (OCV) and cycled cathode composite (cycled between 2.8 – 4.8 V vs Li^+/Li) pellets. Color scale unit: a.u..

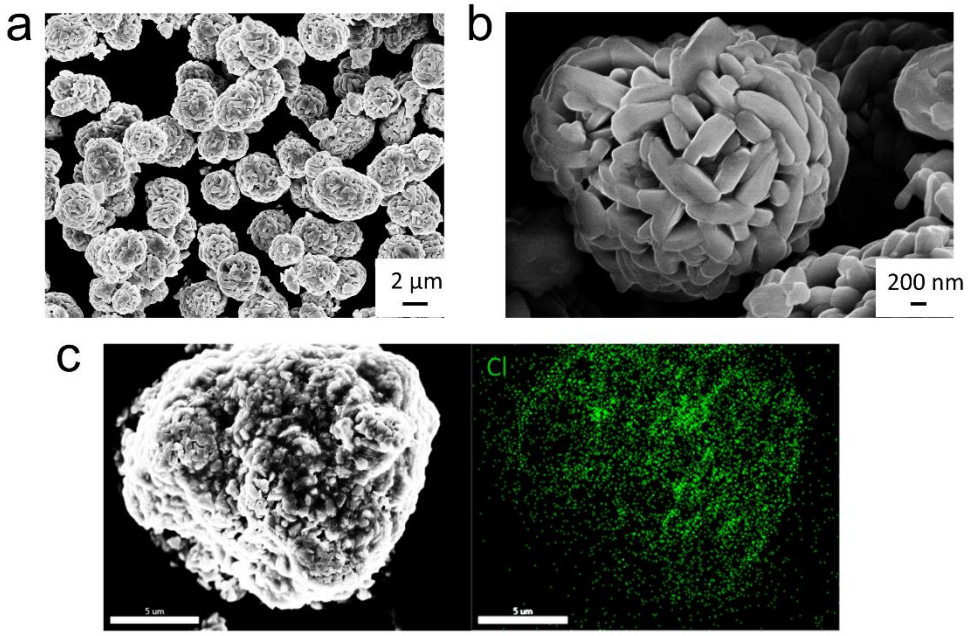

Supplementary Figure 25. SEM images of (a) bare NCM622 and (b) enlarged image of a bare NCM622 particle. (c) Enlarged SEM image of one $Li_2In_{1/3}Sc_{1/3}Cl_4$ coated NCM622 particle. The EDX map (Cl, for simplicity) shows the slightly patchy coating of the chloride solid electrolyte on the surface of the NCM622 particles.

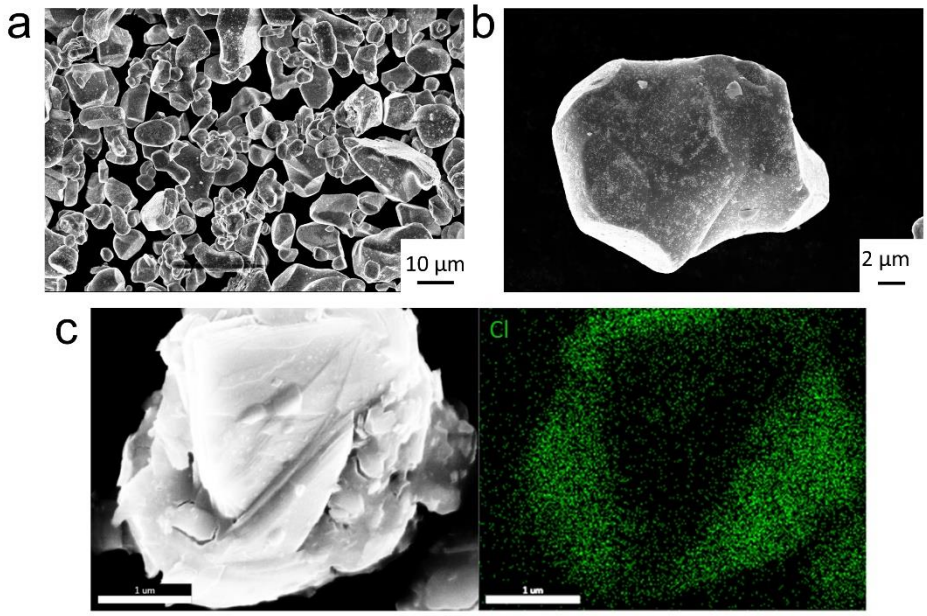

Supplementary Figure 26. SEM images of (a) bare LCO and (b) enlarged image of a bare LCO particle. (c) Enlarged SEM image of one $Li_2In_{1/3}Sc_{1/3}Cl_4$ coated LCO particle. The EDX map (Cl, for simplicity) shows the patchy coating of the chloride solid electrolyte on the surface of the LCO particles.

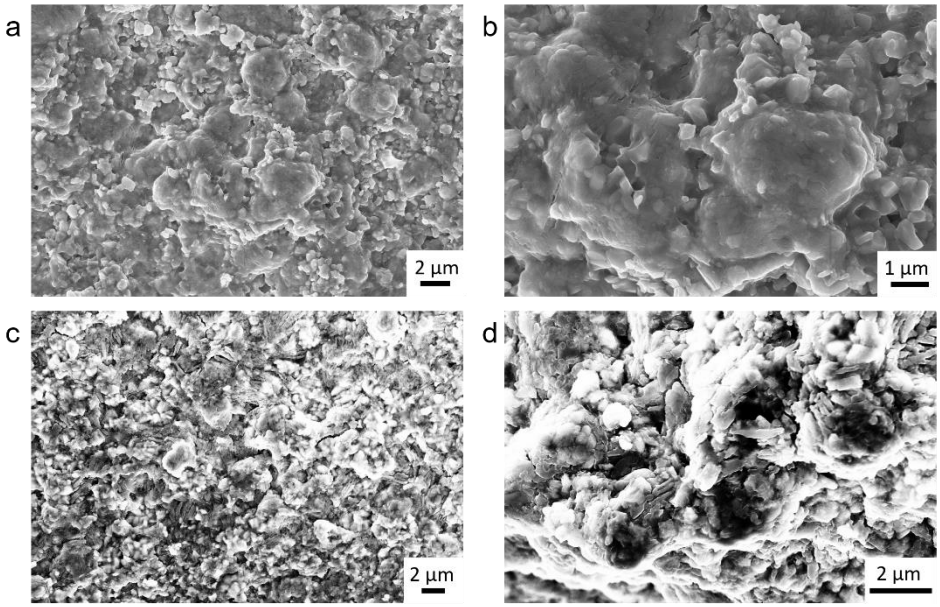

Supplementary Figure 27. Cross-sectional SEM image of the cathode composite of NCM85 ASSBs cycled between 2.8 - 4.3 V vs Li^+/Li at the (a) 3^{rd} charged state and (b) enlarged cross-sectional SEM image, showing no clear void formation between NCM85 particles and SE; and (c) 80^{th} discharged state and (d) enlarged cross-sectional SEM image, showing some crack formation within the cathode composite, but nonetheless good contact between NCM85 and the SE.

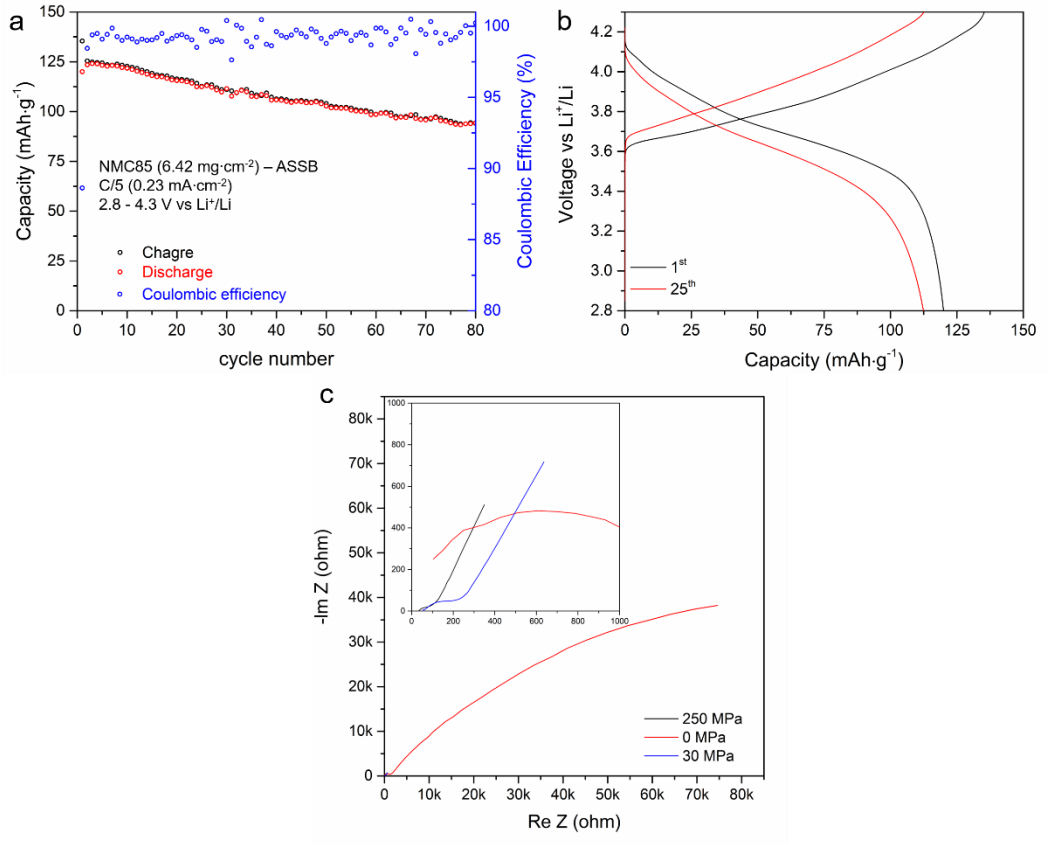

Supplementary Figure 28. (a) Charge-discharge capacity and the coulombic efficiency as a function of cycle number and (b) Charge-discharge voltage profiles for NCM85 ASSB cycled at a C/5 rate between 2.8 - 4.3 V vs Li^+/Li with a much lower applied pressure of 30 MPa during cycling, compared to other cells (cycled at 250 MPa). (c) EIS of the cell before cycling with 250 MPa, 0 MPa and 30 MPa applied pressure, showing the significantly increased cell resistance with lower applied pressure due to poor contact, which explains the lower discharge capacity. The faster capacity fading of cell cycled at 30 MPa compared to the stable cycling of cells cycled at 250 MPa (Figure 4a) demonstrates the importance of high applied pressure to maintain the contact between the CAM and SE to withstand the CAM volume change.

Supplementary Note 6. Applied pressure during cycling is essential to maintain good contact between the CAM and the SE to withstand the CAM volume change. Since various CAMs exhibit different degrees of volume expansion/contraction, an in-depth study of critical pressure for different CAMs is required (beyond the scope of this study) because high applied pressure (even 30 MPa) is not practical. Exploration of new cathode materials with negligible volume change during Li extraction/insertion is needed to reduce the required external cell pressure, along with advances in cell design and architecture.

LIST OF SUPPLEMENTAL TABLES

Supplementary Table 1. Ionic conductivity at room temperature and corresponding activation energy for the materials described in the main text.

Compositions	Ionic conductivity ($mS \cdot cm^{-1}$) ± 0.02	Activation energy (eV)
$Li_2In_{0.111}Sc_{0.555}Cl_4$	1.92	0.34
$Li_2In_{0.222}Sc_{0.444}Cl_4$	1.83	0.32
$Li_2In_{0.333}Sc_{0.333}Cl_4$	1.99	0.33
$Li_2In_{0.444}Sc_{0.222}Cl_4$	2.03	0.34
$Li_2In_{0.555}Sc_{0.111}Cl_4$	1.90	0.35
$Li_2In_{0.666}Cl_4$	1.11	

Supplementary Table 2. Atomic coordinates, occupation factor, and isotropic displacement parameters of $Li_2In_{0.333}Sc_{0.333}Cl_4$ obtained from time-of-flight powder neutron diffraction data collected at 300 K.

a = 10.42138(8) Å, space group: Fd-3m						
Atom	Wyckoff site	x	y	z	Occupancy	U_{iso} (Å^2)
Li1	8*a*	0.125	0.125	0.125	0.28(5)	0.025(12)
Li2	16*c*	0	0	0	0.19(2)	0.034(8)
Li3	48*f*	0.125	0.125	0.89(2)	0.008(7)	0.025
Li4	16*d*	0.5	0.5	0.5	0.675(2)	0.0038(7)
Sc1	16*d*	0.5	0.5	0.5	0.164(1)	0.0038(7)
In1	16*d*	0.5	0.5	0.5	0.161(2)	0.0038(7)
Cl1	32*e*	0.25424(6)	0.25424(6)	0.25424(6)	1	0.0203(2)

Supplementary Table 3. Crystallographic data for $Li_3In_{0.666}Sc_{0.334}Cl_6$ obtained from the single crystal X-ray diffraction study at 270 K.

Crystal data	
Formula	$Li_{2.17}In_{0.66}Sc_{0.34}Cl_6$
Formula weight	319.13
Crystal system	Monoclinic
Space group	*C*2/*m*
a, b, c (Å), beta (°)	6.404(1), 11.066(2), 6.383(1) Å, 109.790(5) °
V (Å^3)	425.64(13)
Z	2
Calc. density (g/cm^3)	2.490
Abs. coef. μ (Mo Kα) (mm^{-1})	3.917
F(000)	296
Color of crystal	Colorless
Crystal size (mm)	0.020 x 0.020 x 0.020
Data collection	
Temperature (K)	270(2)
Radiation (Å)	Mo Kα, 0.71073
Theta range for data collection	3.392 – 29.958°
Index ranges	$-8 \le h \le 6$, $-15 \le k \le 15$, $-8 \le l \le 8$
Reflections collected	2174
Independent reflections	645 (R_{int} = 0.0234)
Completeness to θ = 25.242°	99.5%
Absorption correction	Multi-scan
Max. and min. transmission	0.6330, 0.7460
Refinement	
Refinement method	Full-matrix least-squares on F^2
Data/ restraints/ parameters	645 / 0 / 29
Goodness of fit on F^2	1.110
Final R indicates [$I > 2\text{sigma}(I)$]	R1 = 0.0327, wR2 = 0.0736
R indicates (all data)	R1 = 0.0365, wR2 = 0.0762
Extraction coefficient	n/a
Largest diff. peak and hole	2.351 and -0.986 e.Å^{-3}

Supplementary Table 4. Atomic coordinates, occupation factor and equivalent isotropic displacement parameters of $Li_3In_{0.666}Sc_{0.334}Cl_6$ obtained from single crystal X-ray diffraction at 270 K.

Atom	Wyckoff site	*x*	*y*	*z*	Occupancy	U_{eq} (Å^2)
Li1	4*g*	0.5	-0.1660(7)	0	1	0.030(2)
Li2	4*h*	0	0.170(12)	0.5	0.09(7)	0.05(6) (U_{iso})
In1	2*a*	0	0	0	0.664(7)	0.0143(2)
Sc1	2*a*	0	0	0	0.336(7)	0.0143(2)
Cl1	4*i*	0.7561(2)	0	0.2336(2)	1	0.0202(3)
Cl2	8*j*	0.2410(2)	0.83788(6)	0.2383(2)	1	0.0202(3)

Supplementary Table 5. Anisotropic displacement parameters of $Li_3In_{0.666}Sc_{0.334}Cl_6$ obtained from single crystal X-ray diffraction at 270 K.

Atom	**U11**	**U22**	**U33**	**U23**	**U13**	**U12**
Li1	0.023(4)	0.015(4)	0.056(6)	0.000	0.020(4)	0.000
In1	0.0117(2)	0.0112(3)	0.0213(3)	0.000	0.00711(18)	0.000
Sc1	0.0117(2)	0.0112(3)	0.0213(3)	0.000	0.00711(18)	0.000
Cl1	0.0180(5)	0.0230(5)	0.0225(5)	0.000	0.0108(4)	0.000
Cl2	0.0200(4)	0.0172(4)	0.0219(4)	0.0032(2)	0.0051(3)	0.0040(2)

Supplementary Table 6. Atomic coordinates, occupation factor, and isotropic displacement parameters of $Li_2In_{0.444}Sc_{0.222}Cl_4$ and $Li_3In_{0.666}Sc_{0.334}Cl_6$ obtained from time-of-flight powder neutron diffraction data collected at 300 K. U_{iso} values for the Li1 and Li2 sites in $Li_3In_{0.666}Sc_{0.334}Cl_6$ were refined to be equal and the Sc1 and In1 site occupancies were fixed based on the single crystal results.

Spinel $Li_2In_{0.444}Sc_{0.222}Cl_4$, a = 10.42562(8) Å, space group: Fd-3m						
Atom	Wyckoff site	x	y	z	Occupancy	U_{iso} (Å^2)
Li1	8a	0.125	0.125	0.125	0.28(5)	0.025(13)
Li2	16c	0	0	0	0.20(2)	0.040(9)
Li3	48f	0.125	0.125	0.89(4)	0.008(7)	0.025
Li4	16d	0.5	0.5	0.5	0.673(3)	0.0025(10)
Sc1	16d	0.5	0.5	0.5	0.109(1)	0.0025(10)
In1	16d	0.5	0.5	0.5	0.218(3)	0.0025(10)
Cl1	32e	0.25414(6)	0.25414(6)	0.25414(6)	1	0.0208(2)

Monoclinic $Li_3In_{0.666}Sc_{0.334}Cl_6$, space group: $C2/m$ a= 6.4017(3) Å, b = 11.0596(3) Å, c = 6.3756(2) Å, β = 109.781(4) °						
Atom	Wyckoff site	x	y	z	Occupancy	U_{iso} (Å^2)
Li1	4g	0.5	-0.170(3)	0	0.89(4)	0.040(3)
Li2	4h	0	0.19(2)	0.5	0.61(4)	0.040(3)
In1	2a	0	0	0	0.664	0.0104(8)
Sc1	2a	0	0	0	0.336	0.0104(8)
Cl1	4i	0.7541(8)	0	0.2321(7)	1	0.0139(8)
Cl2	8j	0.2390(6)	0.8382(4)	0.2352(4)	1	0.0197(5)

Supplementary Table 7. Comparison of our work with recent reported representative ceramic ASSBs with high voltage CAMs. Results from our work are shown in bold.

Cathode	Catholyte SE	CAM loading ($mg \cdot cm^{-2}$)	Cut-off voltage vs Li^+/Li (V)	Current density ($mA \cdot cm^{-2}$)	Specific capacity ($mAh \cdot g^{-1}$)	Cyclability
NCM85	**$Li_2In_{1/3}Sc_{1/3}Cl_4$**	**6.21-6.93**	**2.8 - 4.3**	**0.25 (0.2C)** **3.36 (3C)**	**~ 200 (0.2C)** **~ 90 (3C)**	**90% (> 600 cycles, 0.2C)** **80% (>3000 cycles, 3C)**
NCM622	**$Li_2In_{1/3}Sc_{1/3}Cl_4$**	**6.52**	**2.8 - 4.6**	**0.24 (0.2C)**	**194**	**92.8 % (320 cycles)**
NCM85	**$Li_2In_{1/3}Sc_{1/3}Cl_4$**	**6.26**	**2.8 - 4.8**	**0.23 (0.2C)**	**219**	**95% (114 cycles)**
NCM85	**$Li_2In_{1/3}Sc_{1/3}Cl_4$**	**21.5**	**2.8 - 4.3**	**0.5 (0.125C)**	**192**	**100% (80 cycles)**
$LiCoO_2$	**$Li_2In_{1/3}Sc_{1/3}Cl_4$**	**52.5**	**2.8 - 4.3**	**1.2 (C/6, 50**°C)	**85**	**100% (500 cycles)**
$LiCoO_2$[6]	Li_3YCl_6	9.9	2.52 - 4.22	0.135 (0.1C)	117	98.0% (100 cycles)
$LiCoO_2$[7]	$Li_{2.5}Y_{0.5}Zr_{0.5}Cl_6$	8.9	3.0 - 4.3	0.550 (0.5C)	92	90% (200 cycles)
$LiCoO_2$[8]	Li_3InCl_6	9.5	2.52 - 4.22	0.130 (0.1C)	124	77 % (100 cycles)
NCM811[9]	Li_3InCl_6	8.92	2.52 - 4.42	0.130 (0.08C)	150	~100 % (70 cycles)
$LiCoO_2$[10]	Li_3ScCl_6	8.92	2.52 - 4.22	0.13 (0.1C)	126	83% (160 cycles)
s-NCA88[11]	$Li_{2.6}Yb_{0.6}Hf_{0.4}Cl_6$	6.4 (only 48.6wt% CAM in cathode composite)	3.0 - 4.3	0.62 (0.5C)	188	83.6% (1000 cycles)
s-NCA[12]	Li_3YCl_6	7.7	3.0 - 4.3	0.77 (0.5C)	180	67.2% (200 cycles)
c-NCM90[13]	Li_6PS_5Cl	38	2.5 - 4.25	3.2 (0.5C, 60 °C)	146	89% (1000 cycles)
c-$LiCoO_2$[14]	$Li_{9.54}Si_{1.74}P_{1.44}S_{11.7}Cl_{0.3}$	4.9	2.5 - 4.1	12 (18C, 100°C)	115	~75% (500 cycles)
c-NCM622[15]	Li_3PS_4	7-8.4	2.9 - 4.4	0.16-0.19 (0.1C)	136	91% (100 cycles)
$LiCoO_2$[16]	$Li_7La_3Zr_2O_{12}$	No Mention	3.0 - 4.05	(0.05C)	94	88% (100 cycles)
c-NCA[17]	Li_6PS_5Cl	6	2.5 - 4.25	0.110 (0.1C)	140	82% (40 cycles)

s-NCA88 – single-crystalline $LiNi_{0.88}Co_{0.10}Al_{0.02}O_2$

s-NCA – single-crystalline $LiNi_{0.88}Co_{0.11}Al_{0.01}O_2$

c-NCM90 – coated-$LiNi_{0.90}Co_{0.05}Mn_{0.05}O_2$

c-$LiCoO_2$ – coated $LiCoO_2$

c-NCM622 – coated-$LiNi_{0.6}Co_{0.2}Mn_{0.2}O_2$

c-NCA – coated $LiNi_{0.80}Co_{0.15}Al_{0.05}O_2$

Supplementary Table 8. The Maxima, 75th percentile, 50th percentile, 25th percentile and minima in the box plot (Figures 7d-f and Supplementary Figure 22).

		SE	OCV	4.3 V	4.6V	4.8 V
I_{Cl^-}/I_{total} (a.u.)	Maxima (Upper bound of whisker)	2760	3640	3180	3330	3080
	75th percentile (Upper bound of box)	2755	3385	3100	3235	2990
	50th percentile (Median)	2705	3315	2995	3110	2910
	25th percentile (Lower bound of box)	2655	3215	2935	2995	2900
	Minima (Lower bound of whisker)	2570	3110	2880	2890	2860
I_{ClO^-}/I_{total} (a.u.)	Maxima (Upper bound of whisker)	22.3	34.3	32.2	32	37.8
	75th percentile (Upper bound of box)	21.1	29.75	31.45	30.4	32
	50th percentile (Median)	18.4	27.1	30.25	28.8	29
	25th percentile (Lower bound of box)	15.1	26.35	29.65	28.35	27
	Minima (Lower bound of whisker)	11	25.4	28.8	26.8	26.8
I_{ScO^-}/I_{total} (a.u.)	Maxima (Upper bound of whisker)	1.34	1.39	1.08	1.35	1.13
	75th percentile (Upper bound of box)	1.25	1.31	0.99	1.29	1.08
	50th percentile (Median)	1.18	1.26	0.96	1.28	1.05
	25th percentile (Lower bound of box)	1.07	1.16	0.91	1.23	1
	Minima (Lower bound of whisker)	1.04	1.11	0.84	1.18	0.96
I_{LiCl^-}/I_{total} (a.u.)	Maxima (Upper bound of whisker)	58.3	44.5	51.8	45.2	38.8
	75th percentile (Upper bound of box)	55.5	43.8	50.65	43.3	37.9
	50th percentile (Median)	53.55	41.8	48.9	41.75	37.35
	25th percentile (Lower bound of box)	50.95	40.7	46.45	40.75	36.7
	Minima (Lower bound of whisker)	50.2	36.2	45.5	40.1	35.3
$I(InCl_3^-)/I_{total}$ (a.u.)	Maxima (Upper bound of whisker)	1300	1240	1260	1280	1160
	75th percentile (Upper bound of box)	1280	1205	1220	1255	1140
	50th percentile (Median)	1265	1200	1205	1230	1105
	25th percentile (Lower bound of box)	1220	1145	1180	1220	1045
	Minima (Lower bound of whisker)	1180	1060	1150	1180	967
$I(ScCl_2^-)/I_{total}$ (a.u.)	Maxima (Upper bound of whisker)	6.08	6.4	7.75	5.98	6.09
	75th percentile (Upper bound of box)	5.84	5.92	7.66	5.78	5.6
	50th percentile (Median)	5.36	5.52	7.42	5.68	5.15
	25th percentile (Lower bound of box)	5.07	5.45	7.22	5.55	4.97
	Minima (Lower bound of whisker)	4.37	5.38	6.81	5.27	4.69
$I(ScCl_3^-)/I_{total}$ (a.u.)	Maxima (Upper bound of whisker)	194	175	115	163	183
	75th percentile (Upper bound of box)	180	154	109	151	159.5
	50th percentile (Median)	171.5	135.5	101	146.5	142.5
	25th percentile (Lower bound of box)	154.5	130.5	101	138	135.5
	Minima (Lower bound of whisker)	124	122	99.7	132	132

References

[1] Zhang, Y. *et al.* Revealing electrolyte oxidation via carbonate dehydrogenation on Ni-based oxide in Li-ion batteries by in situ Fourier transform infrared spectroscopy. *Energy Environ. Sci*. **13**, 183-199 (2020).

[2] Xue, W. *et al.* Ultra-high-voltage Ni-rich layered cathodes in practical Li metal batteries enabled by a sulfonamide-based electrolyte. *Nat. Energy* **6**, 495-505 (2021).

[3] Yu, Z. *et al.* Molecular design for electrolyte solvents enabling energy-dense and long-cycling lithium metal batteries. *Nat. Energy* **5**, 526-533 (2020).

[4] Fan, X. *et al.* Non-flammable electrolyte enables Li-metal batteries with aggressive cathode chemictries. *Nat. Nanotechnol.* **13**, 715-722 (2018).

[5] Zhang, W. *et al.* Degradation mechanisms at the $Li_{10}GeP_2S_{12}/LiCoO_2$ cathode interface in an all-solid-state lithium-ion battery. *ACS Appl. Mater. Interface* **10**, 2226-22236 (2018).

[6] Asano, T. *et al.* Solid halide electrolytes with high lithium-ion conductivity for application in 4V class bulk-type all-solid-state batteries. *Adv. Mater.* **30**, 1803075 (2018).

[7] Park, K.H. *et al.* High-voltage superionic halide solid electrolytes for all-solid-state Li-ion batteries. *ACS Energy Lett.* **5**, 533-539 (2020).

[8] Li, X. *et al.* Air-stable Li_3InCl_6 electrolyte with high voltage compatibility for all-solid-state batteries. *Energy Environ. Sci.* **12**, 2665-2671 (2019).

[9] Li, X. *et al.* Water-mediated synthesis of a superionic halide solid electrolyte. *Angew. Chem. Int. Ed.* **58**, 16427-16432 (2019).

[10] Liang, J. *et al.* Site-occupation-tuned superionic Li_xScCl_{3+x} halide solid electrolytes for all-solid-state batteries. *J. Am. Chem. Soc.* **142**, 7012-7022 (2020).

[11] Park, J. *et al.* Heat treatment protocol for modulating ionic conductivity via structural evolution of $Li_{3-x}Yb_{1-x}M_xCl_6$ ($M = Hf^{4+}$, Zr^{4+}) new halide superionic conductors for all-solid-state batteries. *Chem. Eng. J.* **425**, 130630 (2021).

[12] Han, Y. *et al.* Single- or poly-crystalline Ni-rich layered cathode, sulfide or halide solid electrolyte: which will be the winner for all-soli-state batteries? *Adv. Energy Mater.* **11**, 2100126 (2021).

[13] Lee, Y.G. *et al.* High-energy long-cycling all-solid-state lithium batteries enabled by silver-carbon composite anodes. *Nat. Energy* **5**, 299-308 (2020).

[14] Kato, Y. *et al.* High-power all-solid-state batteries using sulfide superionic conductors. *Nat. Energy 1*, 16030 (2016).

[15] Kim, A.Y. *et al.* Stabilizing effect of a hybrid surface coating on a Ni-rich NMC cathode materials in all-solid-state batteries. *Chem. Mater.* **31**, 9664-9672 (2019).

[16] Han, F. *et al.* Interphase engineering enabled all-ceramic lithium battery. *Joule* **2**, 497-508 (2018).

[17] Doux, J. M. *et al.* Pressure effects on sulfide electrolytes for all solid-state batteries. *J. Mater. Chem. A* **8**, 5049-5055 (2020).